ZnAl layered double hydroxide based catalysts (with Cu, Mn, Ti) used as noble metal-free three-way catalysts

ZnAl layered double hydroxide based catalysts (with Cu, Mn, Ti) used as noble metal-free three-way catalysts

Tim Van Everbroeck*[1], Jianxiong Wu[3], Daniel Arenas-Esteban[4], Radu-George Ciocarlan[1], Myrjam Mertens[2], Sara Bals[4], Christophe Dujardin[3], Pascal Granger[3], Elena M. Seftel[2], Pegie Cool[1]

[1] *Laboratory of Adsorption and Catalysis, University of Antwerp, Universiteitsplein 1, 2610 Wilrijk, Belgium.*

[2] *VITO Flemish Institute for Technological Research, Boerentang 200, 2400 Mol, Belgium*

[3] *Univ. Lille, CNRS, Centrale Lille, Univ. Artois, UMR 8181 - UCCS - Unité de Catalyse et Chimie du solide, F-59000 Lille, France*

[4] *Electron Microscopy for Materials Research (EMAT) and NANOlab Centre of Excellence, University of Antwerp, Groenenborgerlaan 171, 2020, Antwerp, Belgium*

**corresponding author: tim.vaneverbroeck@uantwerpen.be*

Abstract

This research presents a novel approach for developing noble metal-free three-way catalysts by using ZnAl layered double hydroxide (LDH) co-precipitated with Mn and Ti. Cu was added as the catalytically active metal. Two methods were explored, namely the addition of Cu during the co-precipitation step and a post-synthesis method using the LDH memory effect. In case the starting material had LDH characteristics high amounts of CuO were adsorbed on the support and high dispersion degrees of CuO were obtained. A four-cycle three-way catalysis test was used for evaluation. The smaller CuO particle size resulted in better performance for oxidation reactions. The addition of Mn had a positive effect on the general performance of the catalysts, while the presence of Ti mainly improved the NO conversion.

The developed materials showed good stability in consecutive catalytic testing cycles and even show some NO conversion under stoichiometric conditions. The developed CuO-based ZnAl layered double hydroxide-based materials are very promising catalysts for Three-way catalysis, allowing to reduce the precious metal content compared to the classical catalysts composition.

Keywords

Layered Double Hydroxides, memory effect, three-way catalysts, copper oxide, NO reduction, CO oxidation

Highlights

- High loadings of well-dispersed CuO nanoparticles on layered double hydroxide (LDH)
- Superior catalytic performance due to well-dispersed CuO nanoparticles
- Amorphous aluminium oxide in the LDH material works as support dispersing CuO
- Increased performance with Mn addition and NO conversion with Ti addition

Introduction

While the technology for the production of alternatively powered vehicles has greatly advanced in the past few years and the sales of diesel cars continues to fall, only 10.5 % of the passenger cars registered in 2020 in the European Union relied only on electricity (European Automobile Manufacturers Association, 2021). Petrol cars are equipped with a three-way catalytic converter whose function is to remove CO, NO_x and hydrocarbons. The key components of current three-way converters are the precious metals Pt, Pd, and Rh (Kašpar et al., 2003; Kumar et al., 2017). These materials are however considered as critical raw materials (CRM) because of their great economic importance, while their supply is at risk. This

means that their use in new technologies must be limited as much as possible (European Commission, 2018). This also causes a revived interest in the use of alternative materials to replace the CRMs.

Although having a reaction rate of about 50 times lower than Pd for CO (Kummer, 1980), CuO is the preferred catalyst to focus on as it is not a CRM (European Commission, 2018). While lower reaction rates could be compensated by using larger amounts of CuO, a good dispersion is essential for the catalytic activity of CuO, which is challenging to achieve with larger amounts on a given surface area (Bennici et al., 2004). At the same time, large amounts of CuO can agglomerate easier when exposed to the high temperatures of the exhaust gas. In order to avoid this, it is important to design a catalyst with a high surface area, while having highly dispersed CuO deposited on the surface of the support. Another way of increasing or changing the catalytic properties of a material is by the addition of a co-catalyst material. Specific metal oxides can work together in a synergetic system, leading to a better performance than the sum of the separate materials (Cavani et al., 1991; Weng and Delmon, 1992; Liu et al., 2019). These mixtures of metal oxides (MO) will be exposed for a long time at high temperatures, under different gas mixtures, and the formation of mixed metal oxides (MMO), such as spinels and perovskites, is likely to occur. This can directly influence the performance of the catalyst (Cousin and Ross, 1990).

In this work, layered double hydroxide (LDH), with different compositions, are synthesized and used as precursors to further tune three-way catalyst compositions of MMOs. MMOs derived from LDH are particularly interesting in catalytic applications due to their large surface area, homogeneous distribution of the different components and basic character (Cavani et al., 1991; Gennequin et al., 2010; Kowalik et al., 2013; Mrad et al., 2015). The LDH structure

consists of positively charged hydroxide layers, resulting from the mixture of divalent (such as Mg^{II} or Zn^{II}) and trivalent (such as Al^{III}) or tetravalent atoms (such as Ti^{IV}) (Saber and Tagaya, 2003, 2008; E. M. Seftel et al., 2008; Li et al., 2017) with interstitial layers of anions (such as CO_3^{2-}) that compensate for the positive charge of the metal hydroxide layers (Gennequin et al., 2010). Furthermore, water molecules are also located in the interstitial layers (Cavani et al., 1991). One of the most interesting properties of the LDH is that after calcination, the resulted MMO-type material is able to reconstruct the original LDH structure as soon as the materials are brought into contact with water and an anion source. The phenomenon is often referred to as "the memory effect" (Cavani et al., 1991; Marchi and Apesteguía, 1998; Erickson et al., 2005; Carja et al., 2010; Gennequin et al., 2010; Kowalik et al., 2013).

Cu(O) was used as the main active material and was either inserted in the material during the initial LDH synthesis via co-precipitation or afterwards in an impregnation step by making use of the "memory effect" property of LDH.

While the most common LDH consist of Mg and Al (Cavani et al., 1991), this research is based on Zn and Al LDH in a 2:1 ratio. Here, Zn was chosen mainly for its structural role in the LDH synthesis as well as its beneficial synergistic effect for CO oxidation when used together with Cu and Ti (Saber and Zaki, 2014). Zn was partially substituted by Cu in a molar ratio of 1:1, as this is the maximal amount of Cu that could be isomorphously substituted within the hydroxyl layers of LDH. Promising research results for CO oxidation (Saber and Zaki, 2014) and NO reduction (Yuan et al., 2013, 2014; Chen et al., 2014) were reported by using LDH based catalysts featuring Ti. Therefore, several compositions of LDH containing Ti were further prepared by the isomorphous substitution of trivalent Al^{III} atoms with tetravalent Ti^{IV} atoms in order to improve the performances of the three-way MMO catalysts. Furthermore,

different formulations with Mn were synthesized, based on the promising research towards NO_x abatement of the Mn containing LDH (Obalová et al., 2007, 2009; Li et al., 2010, 2012; LI et al., 2014; Pacultová et al., 2016).

The aim of this work is two-fold. Firstly, to show how LDH can be used as a basis for the development of Cu-based three-way catalysts and that the reconstructive properties of LDH can be utilized to further optimise CuO nanoparticles on the surface of the material as opposed to the traditional co-precipitation. Secondly, to assess how different metals (Mn, Zn, Al, Ti) influence the catalytic performance of CuO by interacting with it or by forming mixed metal oxides.

Experimental

Catalyst preparation

Two synthesis strategies were explored for the preparation of copper-containing three-way catalysts, e. g. direct co-precipitation at constant pH and reconstruction route by taking advantage of the memory effect property of the LDH, respectively. The commercial benchmark reference catalysts (0.5% $Pd/CeZrO_2$ and "TWC", a grounded commercial three-way catalyst) have been supplied by Johnson Matthey, UK.

a) Co-precipitation method

The initial materials were synthesized by a common co-precipitation method for LDH, at fixed pH. In a typical synthesis, 120 mL of a solution of the mixed metal salts was prepared by dissolving the metal salts listed in the supplementary information in the appropriate amount of water for a total concentration of 0.5 M. The molar ratios of the metals were according to **¡Error! No se encuentra el origen de la referencia.**. The resulting mixed metals solution was

mixed with 40 mL of a 1 M Na_2CO_3 solution and was added dropwise and simultaneously with a 2 M NaOH solution to a beaker while stirring. The flow of the two solutions was regulated as such to maintain the pH value at 7.5. The obtained precipitate was aged under stirring for 24 h at room temperature. The obtained precipitate was collected by vacuum filtration, washed thoroughly with water and dried overnight in an oven at 80°C(E. M. Seftel et al., 2008; E. Seftel et al., 2008).

For simplicity reasons, the synthesized materials are labelled based on the elements in their composition. The names of the samples and the ratios between the elements are displayed in Table 1.

Sample name	Elements	Atomic ratio
ZA	Zn, Al	2:1
ZCA	Zn, Cu, Al	1:1:1
ZAT	Zn, Al, Ti	4:1:1
ZCAT	Zn, Cu, Al, Ti	2:2:1:1
MZAT	Mn, Zn, Al, Ti	2:2:1:1
MCAT	Mn, Cu, Al, Ti	2:2:1:1
MA	Mn, Al	2:1
MT	Mn, Ti	2:1

Table 1: Composition details of the catalysts prepared via the co-precipitation method.

b) Reconstruction method

By following the same procedure described above, copper-free LDH were also prepared and further used to explore the second synthesis strategy based on the memory effect.

These materials were calcined at 400°C for 4 h (ramping speed of 1°C/min), followed by a slow cooling down to room temperature. 1 g of these MMOs were suspended into 250 mL of 0.1 M copper acetate solution under stirring for 30 minutes to allow the reconstruction of the initial layered structure and intercalate the copper acetate anions. Finally, the solid fraction was separated by centrifugation, washed thoroughly with water and dried overnight in an oven at 80°C (Carja et al., 2013).

The materials after calcination are additionally labelled with the temperature details (for example "-400"). The materials that were impregnated with Cu according to the reconstruction method are indicated with "C/" before their name.

Finally, all the copper-loaded materials, as prepared by the two strategies as described above, were calcined at 600°C for 4 h (ramping speed of 1°C/min) before their use in the catalytic experiments.

Physicochemical characterisation

The materials were characterized by X-ray powder diffraction (XRD) using an X-ray diffractometer (PANalytical X'Pert PRO MPD) equipped with CuKα radiation (λ = 0.15406 nm). The analysis was performed from 2θ = 5 – 70° with a scanning speed of 0.04°/4s. The average crystallite size was estimated using the Scherrer equation, which is explained in the supplementary information.

N_2-physisorption was carried out at -196°C on a Quantachrome Quadrasorb SI automated gas adsorption system. Prior to the measurements, the samples were outgassed at 60°C for 16 h except for the materials calcined at 400 or 600°C. These were outgassed at 200°C for 16 h. The specific surface area was calculated using the Brunauer-Emmet-Teller (BET) equation. The

Barret-Joyner-Halenda (BJH) method was applied to estimate the pore size distribution. The total pore volume was determined at P/P_0= 0.95.

SEM-EDX was used to determine the surface composition, using a FEG-ESEM-EDX, FEI Quanta 250 by scanning the whole field instead of discrete points.

TEM characterization of CuO nanoparticles was performed by high-angle annular dark field scanning transmission electron microscopy (HAADF-STEM) and energy dispersive X-ray spectroscopy (EDS) using an aberration-corrected cubed FEI Titan microscope equipped with a Super X EDS detector operating at 300 kV.

Catalytic activity measurements

The catalytic tests were performed in a quartz fixed bed reactor. In a typical experiment, 0.200 g of the powder catalyst (100 - 200 μm) was mixed with 0.200 g silicon carbide to avoid limitations related to mass and heat transfer phenomena. The catalytic performance was evaluated from the conversions of the different gases in a multi-cycle temperature-programmed experiment. The course of the temperature as a function of time during the experiment is illustrated in Supplementary Figure 1, in a relevant time-scale. More details can be found in the supplementary information.

Results

Structural characterization and crystallinity of the catalysts

With X-ray diffraction (XRD) the crystal structures of the catalysts through the different steps of the synthesis can be identified. Using the Scherrer equation, the average CuO crystallite size is estimated from the (111) reflection at 38.7° and reported inTable 2. Porosity analysis of the catalysts was performed by N_2-sorption. The isotherms along with the surface area of the

materials throughout the different steps of the synthesis are presented in the supplementary information.

Cu loading on ZnAl-LDH

The X-ray diffractograms of C/ZA and ZCA through the different steps of the synthesis are presented in Figure 1. In both the materials after co-precipitation (ZA and ZCA) the typical diffraction patterns for a ZnAl carbonate intercalated layered double hydroxide (LDH) (PDF 01-075-2983 (Gates-Rector and Blanton, 2019)) are present. The typical (003) and (006) basal reflections centred at 11.7 and 23° are associated with the stacking of the layers (Cavani et al., 1991).

The calcination of ZA at 400°C leads to the collapse of the LDH structure and ZnO is crystallised, which is observed by it's typical pattern (Zincite, PDF 00-036-1451 (Gates-Rector and Blanton, 2019)). After the reconstruction method, the structural reconstruction is confirmed by the reappearance of the typical LDH refection planes in the XRD pattern in the forthcoming Cu-containing material, C/ZA. The reflections are however shifted in comparison to the original materials, especially the (003) diffraction plane. For the LDH materials, this diffraction plane is used to calculate the interlayer distance in the structure, providing direct information of the anions identity and orientation within the interlayer gallery. For example, in the case of ZA, the interlayer distance is 0.76 nm (d_{003}) typical for the carbonate-containing LDH, while for C/ZA it has increased to 1.25 nm (d_{003}) which indicates the intercalation of the acetate anions during the reconstruction process in the presence of copper acetate aqueous solution (Prevot et al., 2008). At the same time, for C/ZA, the reflection at 11.7° (d_{003}) occurs, which corresponds to the original carbonate LDH structure.

The three-way catalysts are obtained after calcination at 600°C. Both cases (C/ZA-600 and ZCA-600), feature the XRD patterns of CuO (tenorite, PDF 45-937) as well as of ZnO together with a spinel phase. The general formula for a spinel structure is $A^{2+}B^{3+}{}_2O_4$ (A – tetrahedral site, B – octahedral site). The atomic ratio for spinel generally is M^{2+}:M^{3+} = 1:2 as compared to M^{2+}:M^{3+} = 2:1 for the LDH (Cavani et al., 1991; Zhao et al., 2017). This means that there will be anyway a surplus of M^{2+} if the LDH is completely transformed into spinel, and this is confirmed by the ZnO or CuO formation in the calcined materials. The spinel phase can be associated with $ZnAl_2O_4$ (PDF 00-005-0669). However, after the calcination at 600°C, a limited amount of copper can penetrate the spinel structure by substituting one of the elements in the octahedral or tetrahedral sites. Due to the fact that Cu and Zn have similar values of ionic radius, it is very difficult to make a distinction between the two atoms within the spinel phase based on the XRD patterns.

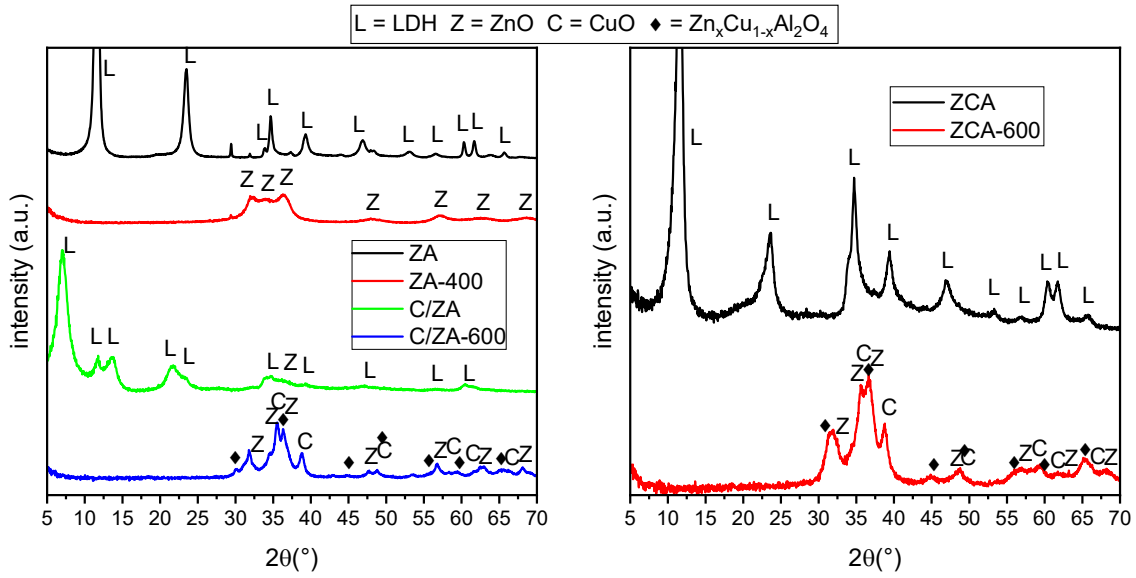

Figure 1: X-ray diffractograms at different stages of the synthesis of C/ZA (left) and ZCA (right). ZA and ZCA are obtained by co-precipitation. Cu-containing C/ZA is obtained by the reconstruction method. Note: the intensity of the diffractogram of ZA has been divided by 2 in order to be displayed together with the others.

Cu loading on ZnAlTi-LDH

The diffractograms of C/ZAT and ZCAT at the different stages of the synthesis are compared in Figure 2. Once more, in both ZAT and ZCAT the typical pattern of LDH after co-precipitation is present. Upon calcination at 400°C, ZAT loses the LDH structure with the concomitant formation of the ZnO phase. The reconstruction process in the presence of the copper acetate solution leads to the intercalation of the acetate anions within the interlayer gallery of the obtained LDH (C/ZAT). Further calcination at 600°C of the materials obtained by both co-precipitation and reconstruction (C/ZAT-600 and ZCAT-600) are characterized by similar XRD patterns with the features of CuO and ZnO combined with a $ZnAl_2O_4$ spinel phase. Due to the additional presence of the Ti^{4+} cations within the LDH phase, the concomitant formation of a Zn_2TiO_4 phase was further identified (PDF 01-082-1438 (Gates-Rector and Blanton, 2019)).

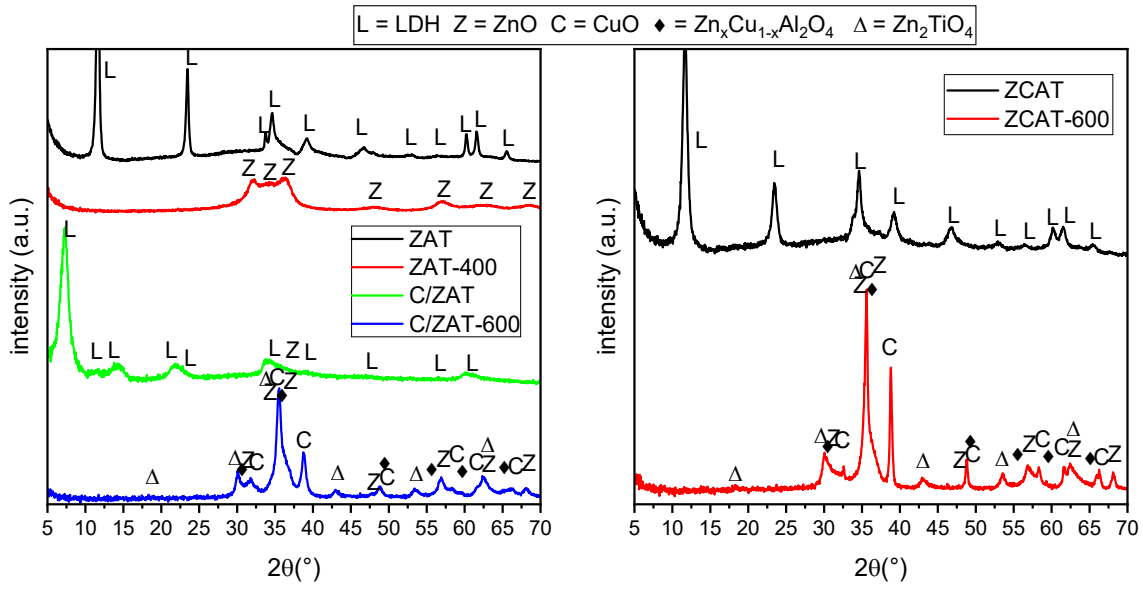

Figure 2: X-ray diffractograms at different stages of the synthesis of C/ZAT (left) and ZCAT (right). ZAT and ZCAT are obtained by co-precipitation, while C/ZAT contains Cu deposited by the reconstruction method.

Cu loading on MnZnAlTi-LDH and MnCuAlTi-LDH

The diffractograms of C/MZAT and MCAT in the different stages of the synthesis are displayed in Figure 3. Less intense XRD diffraction lines characteristic to the LDH phase may be identified

for the as-prepared MZAT and MCAT material via the co-precipitation method. As such, the (003) reflection characteristic to the LDH phase may be identified together with the reflections of a $MnCO_3$ (Rhodochrosite, PDF 01-073-4352 (Gates-Rector and Blanton, 2019)) phase. Upon calcination of the MZAT material at 400°C, the Zn_2TiO_4 phase is formed, which in the case of the previously discussed ZAT material was not formed at this stage of the synthesis. Furthermore, when the reconstruction procedure is applied, ZnO particles combined with a $ZnMn_2O_4$ (Hetaerolite, PDF 00-024-1133) phase are formed (C/MZAT). Therefore, for this initial metal composition in the LDH structure, the reconstruction process via the memory effect property was not achieved, probably due to the low crystallinity of the initially obtained layered structure and as well as the presence of the additional $MnCO_3$ phase. Further calcination at 600°C leads to very significant differences between the obtained three-way catalytic materials, e. g. the C/MZAT-600 and the MCAT-600, respectively. This can be attributed to the presence of Zn. In the XRD pattern of C/MZAT-600 all the peaks may be associated to structures that contain Zn, namely Zn_2TiO_4, $ZnMn_2O_4$ and ZnO, respectively, while in the case of MCAT-600 these structures are not formed due to the absence of Zn ions in the initial synthesis mixtures. The presence of Cu containing phase and its content is proven by measuring SEM-EDX as it will be discussed in a later section. In the latter case, a spinel-like phase, identified as $Cu_{1.5}Mn_{1.5}O_4$ (PDF 01-070-0262), is formed from the reaction of the high amounts of Mn_2O_3 and CuO, which is in agreement with previously reported studies in literature (Blasse, 1966; Vandenberghe et al., 1973, 1976; Behar et al., 2012; Biemelt et al., 2016; Van Everbroeck et al., 2020).

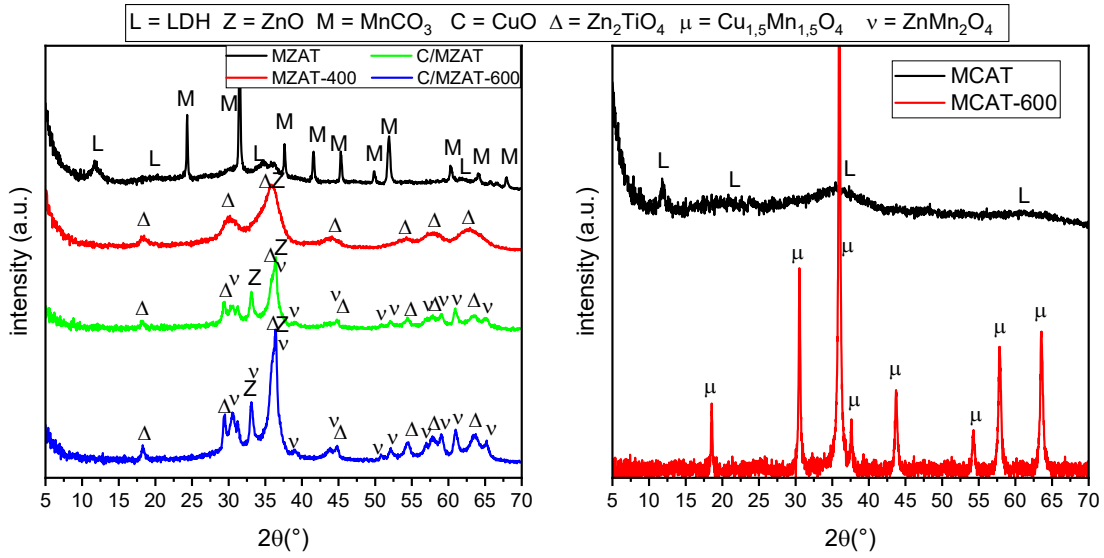

Figure 3: X-ray diffractograms at different stages of the synthesis of C/MZAT (left) and MCAT (right). MZAT and MCAT are obtained by co-precipitation. Cu-containing C/MZAT is obtained by the reconstruction method.

Cu loading on MnAl and MnTi-LDH

According to the diffractograms of C/MA and C/MT at the different stages of the synthesis, in neither of the materials the LDH structure was formed after co-precipitation (Figure 4). As a consequence, no LDH structures were formed after the reconstruction step. The only crystalline structure in the co-precipitated materials was $MnCO_3$, together with some $Al(OH)_3$ (Bayerite, PDF 01-077-0250 (Gates-Rector and Blanton, 2019)) in the case of the as-synthesized MA material. Calcining at 400°C and applying the reconstruction procedure leads to very similar materials. There are still some remnants of the $MnCO_3$ phase together with MnO_2 (Akhtenskite, PDF 01-089-5171 (Gates-Rector and Blanton, 2019)). Finally, the heat treatment of the catalysts at 600°C leads to the transformation of the MnO_2 phase into a mixture of Mn_2O_3 (Bixbyite PDF 31-825) and Mn_3O_4 (PDF 86-2337), while there is no indication of a spinel phase formation, such as $Cu_{1.5}Mn_{1.5}O_4$ in the XRD patterns. A TiO_2 rutile phase (PDF 00-021-1276) can additionally be found in MT-600.

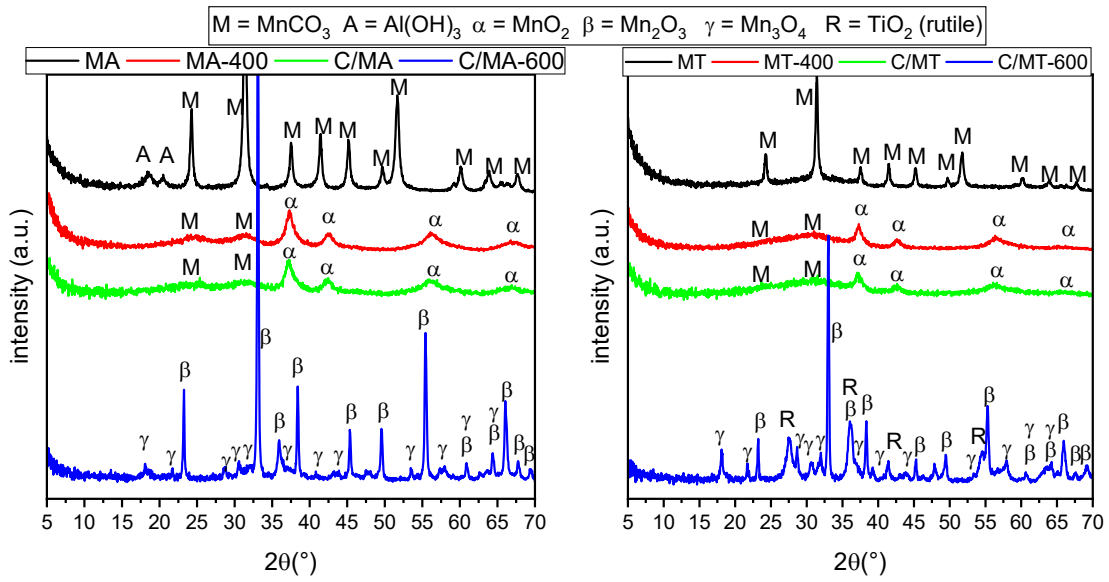

Figure 4: X-ray diffractograms at different stages of the synthesis of C/MA (left) and C/MT (right). MA and MT are obtained by co-precipitation and C/MA contains Cu deposited by the reconstruction method.

Quantification of Cu loading in the three-way catalysts

The Cu content of the final materials as determined by SEM-EDX and the average CuO crystallite size before and after the catalytic test is summarized in Table 2. The Cu content is around 35-40% for the materials that had Cu included in the first co-precipitation synthesis step (ZCA-600, ZCAT-600 and MCAT-600), but it is further increased by applying the reconstruction synthesis route on the calcined LDH materials C/ZA-600 and C/ZAT-600. Lower copper loadings are achieved in the case of the parent materials that did not display the characteristics of a well-layered structure after the co-precipitation process, such as C/MZAT, C/MA and C/MT. The precursors used in their preparation did not present only an LDH-type structure but a combination with other crystalline phases or sometimes a more amorphous character. It should be noted that, for all the prepared catalysts, the exact same concentration of copper acetate solution is used. Large variations in the crystallites sizes of the CuO nanoparticles, e. g. 7 nm and 26 nm, respectively occur in ZCA-600 and ZCAT-600 prepared via the co-precipitation method. On the other hand, by following the reconstruction method,

similar sizes of the CuO crystallites of ±10 nm, are achieved, namely for the C/ZA-600 and C/ZAT-600 three-way catalysts. After the catalytic test, the CuO crystallite sizes increase for most of the materials, except for ZCAT-600. While 18 nm CuO crystals are formed for MCAT-600 after the test, no CuO crystals are XRD discernible in any of the other Mn-containing materials, indicating that these CuO crystallites have sizes that are probably below 3 nm.

Sample	Cu content (wt%)	CuO crystallite size (before cat. test) (nm)	CuO crystallite size (after cat. test) (nm)
ZCA-600	37	7	14
C/ZA-600	62	11	15
ZCAT-600	35	26	21
C/ZAT-600	56	10	15
MCAT-600	41	-	18
C/MZAT-600	10	-	-
C/MA-600	11	-	-
C/MT-600	11	-	-

Table 2: Cu content and estimated CuO crystallite size of the final materials (before and after the catalytic test). Copper content determined by SEM-EDX. CuO size calculated with the Scherrer equation.

Energy-dispersive X-ray spectroscopy (STEM-EDS) maps were acquired from different areas on samples ZCAT-600, C/ZAT-600 and C/MA-600 to further investigate the size of the CuO nanoparticles and their distribution. Figure 5 shows HAADF-STEM images and their respective elements composition, obtained on representative areas for each sample. Whereas for ZCAT-600 and C/ZAT-600 samples it is easy to find isolated zones that clearly indicate the presence

of Cu (Figure 5b, d), such areas are absent in the C/MA-600 sample due to a high degree of agglomeration between particles. Even so, some isolated CuO nanoparticles are marked in Figure 5f with red circles. CuO nanoparticles adopt a rectangular shape in all three cases, with an average nanoparticle size, determined by STEM-EDS, of 35 ± 17 nm, 15 ± 11 nm and 20 ± 8 nm for the ZCAT-600, C/ZAT-600 and C/MA-600 composites respectively (see Supplementary figure 8). These values do not exactly match the sample size obtained in bulk, which can be understood since TEM is a very local technique. Nevertheless, the particle size trend is confirmed, with bigger particles for the ZCAT-600 sample in comparison to the C/ZAT-600. On the other hand, for the C/MA-600 sample, CuO nanoparticles are observed in small quantities, which explains why they are not detected by XRD.

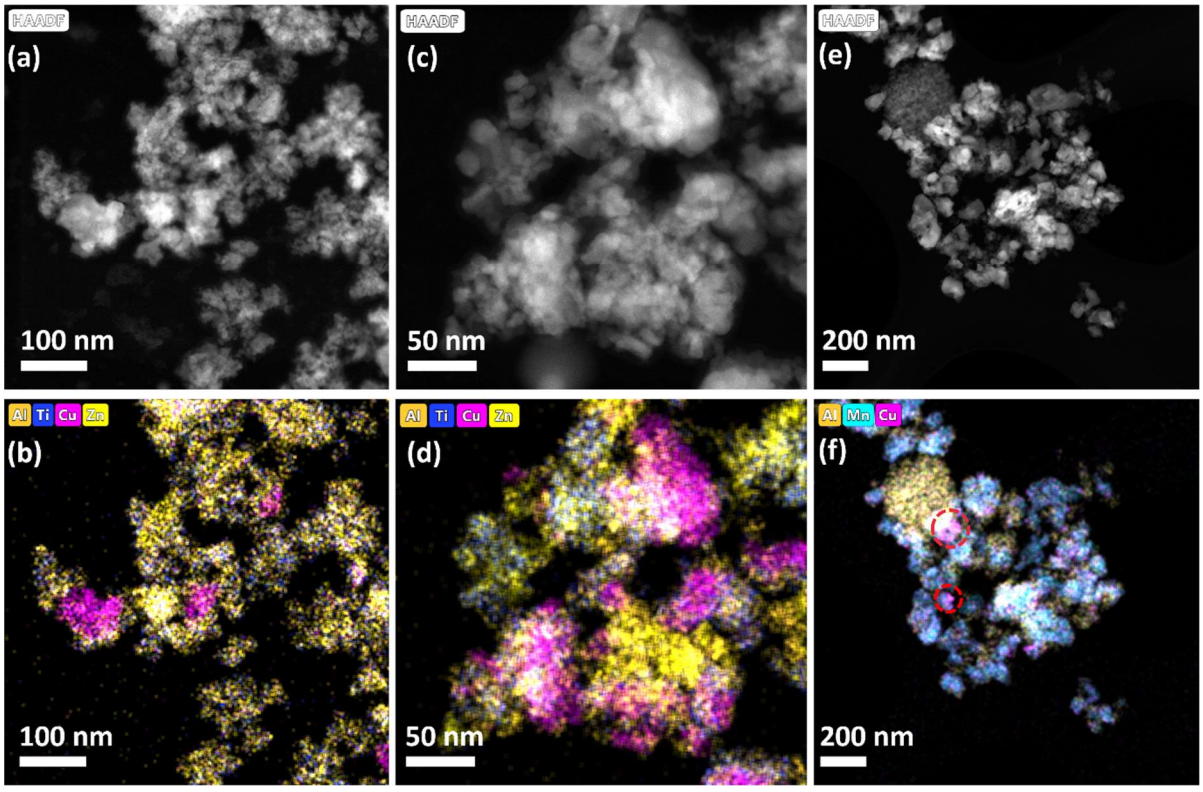

Figure 5: HAADF-STEM images and their respective EDS elemental distribution for (a, b) ZCAT-600, (c, d) C/ZAT-600 and (e, f) C/MA-600 composites. For the EDS maps, Al is marked in brown, Ti in dark blue, Cu in pink, Zn in yellow and Mn in light blue.

Catalytic activity testing

As described in the experimental section, the catalytic test consists of four heating and cooling cycles in three different gas compositions, after an initial pre-treatment cycle. The conversions of NO, CO, propene (C_3H_6) and propane (C_3H_8) as a function of temperature during heating in the different cycles are displayed in Figure 6 and Supplementary Figure 9 to 11. The temperatures at which 50% conversion (Light-off temperature, T_{50}) is reached and, in case of the NO conversion, the maximal conversion and temperature at which this conversion is reached can be found in tables in the supplementary info. Light-off temperatures at 50% conversion are typically used in temperature-programmed experiments to indicate the onset temperature of significant catalytic activity (Biasin et al., 2019).

In the first stoichiometric cycle (Figure 6Figure 6), NO conversion generally does not reach over 10%. All the NO conversions display local maxima, only for C/MA-600 the NO conversion keeps rising until the end of the measurements. The maximum NO conversion is notably higher for C/ZAT-600, C/MZAT-600, C/MA-600 and C/MT-600. The temperature of 50% CO conversion is the lowest for C/MA-600, C/MT-600 and C/MZAT-600, while ZCAT-600 differentiates the most from the others for a much higher T_{50}. On the other hand, the propene conversion curves are much more diverse. While C/MZAT-600 and C/ZAT-600 have a T_{50} around 330 and 350°C, C/MT-600 and MCAT-600 only reach this above 520°C. Propane conversion generally only starts above 500°C. The only exception is in the case of C/MA-600, which reaches even 50% under 500°C.

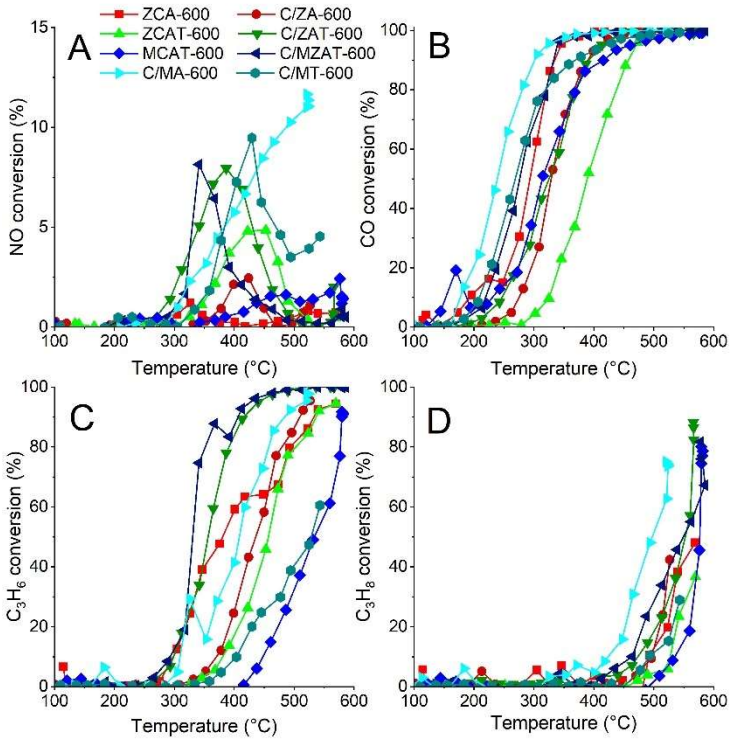

Figure 6: Temperature programmed conversion curves under stoichiometric conditions, first cycle, A: NO conversion, B: CO conversion, C: propene conversion, D: propane conversion.

Discussion

Layered double hydroxides have been successfully formed even if the Zn^{II} atoms were partially substituted by Cu^{II} or Al^{III} atoms are partially substituted by Ti^{IV}, in both cases for a substitution degree of 50 mol%. The incorporation of large quantities of Mn atoms in the LDH structure is however not as straightforward, due of the fact that Mn atoms lead to octahedral distortions (similarly to Cu atoms) as a result of the Jahn-Teller effect (Cavani et al., 1991; Fridrichová et al., 2017). In the cases of MCAT and MZAT, there is still evidence of the LDH structure, but the experiments prove that Cu or Zn are essential to form the LDH structure with Al (and Ti). Aisawa *et al.* reported that when CO_3^{2-} is used as the anion source for the synthesis of Mn-Al LDH, the LDH could still be formed but $MnCO_3$ could also be formed, which is indeed the case here (Aisawa et al., 2002).

345 While no indications of the LDH-like structure after calcination at 400°C in the XRD results, the
346 LDH structure is reformed after suspension in an aqueous copper acetate solution, even after
347 a long time at ambient conditions. The experiments prove that it is essential for the LDH
348 structure to have a high crystallinity for the starting material in order to exhibit these
349 reconstructive properties. In the case of MZAT, the low intensity of the LDH characteristic XRD
350 reflections as well as the presence of the $MnCO_3$ segregated phase indicate that the material
351 is very unlikely to reconstruct. Accordingly, the materials that do not have the LDH structure
352 before calcination will also not form LDH-like structures when mixed with the copper acetate
353 solution. Besides the characteristic (003) plane of acetate intercalated LDH, the XRD patterns
354 of C/ZA show (Figure 1) another reflection maximum at 11.7°, characteristic to the original
355 carbonate LDH. This can be related to the presence of CO_2 in the air or CO_2 in the aqueous
356 acetate solution (Stanimirova and Balek, 2008).

357 The current experiments suggest that the reconstructed LDH materials are able to take-up
358 large amounts of copper between their layers. After all the synthesis steps, the materials with
359 LDH structure retain up to 6 times more copper (around 60 wt%) than those without LDH
360 structure (around 10 wt%) (Table 2). The thermal decomposition of LDH generally consists out
361 of two phases. At around 200°C the interstitial water is lost, while between 300 and 450°C
362 generally the hydroxyl groups and carbonate are removed (Reichle et al., 1986). From XRD, it
363 is observed that at 400°C some oxides such as ZnO are already crystallised, but the mixed
364 oxides, such as spinels are not yet detectible in the XRD patterns. This means that the mixed
365 oxides are still amorphous, so the lamellar microstructure of LDH is still there, albeit not as
366 crystalline to be discernible with XRD. These LDOs (layered double oxides) obtained by
367 calcination at mild temperatures are known to be very effective to intercalate anions via the
368 reconstruction based on the memory effect mechanism (Seftel et al., 2018). Although it seems

counterintuitive, LDH are also able to adsorb metal cations from a solution. This can occur through multiple mechanisms such as precipitation, surface complexation, isomorphic substitution or chelation (Liang et al., 2013). It can be stated that the intercalation of the anionic species occurs concomitantly with the rehydroxylation of the brucite-like layers. As such, the presence of the hydroxyl groups on the surface of the LDH enables all these mechanisms, explaining why the materials that did not exhibit LDH characteristics in this study did not take up high amounts of Cu^{II}. To determine the exact mechanism that takes place in the experiments more research is needed, which is beyond the scope of the current study.

The estimated CuO crystallite size is much larger for ZCAT-600 in comparison to the other catalysts, while the Cu content is much lower in ZCAT-600 than in C/ZAT-600 and C/ZA-600 (Table 2). This seems to suggest that the reconstruction method leads to much better dispersed CuO in the final material, than by adding copper during the LDH synthesis via the direct co-precipitation route. On the other hand, ZCA-600 contains about the same amount of copper as ZCAT-600, but the CuO size is considerably smaller. For the calcined catalysts, Cu is also likely to be found in the mixed oxide phases (such as $ZnAl_2O_4$ and Zn_2TiO_4) explaining the difference between ZCAT-600 and ZCA-600; Cu is likely to form $CuAl_2O_4$ or together with zinc in a $Zn_xCu_{1-x}Al_2O_4$ spinel after calcination at high temperature (Friedman et al., 1978; Mista et al., 2003; Patel et al., 2015, 2017). This is certainly the reason why no CuO phase could be detected in MCAT-600 by XRD analysis. When mixed together, the solid-state reaction between the CuO and Mn_2O_3 is very likely to form a spinel phase even at temperatures lower than 600°C (Vandenberghe et al., 1973; Van Everbroeck et al., 2020). For C/MA-600 and C/MT-600, the measured copper content is low, resulting in CuO nanoparticles not being detectable by XRD analysis (Figure 4). However, after the catalytic tests, the crystallite size of CuO has increased in some of the catalysts due to the sintering process. Interestingly, in the case of

393 ZCAT-600, there is even a slight decrease of CuO crystallite size; this could be possibly
394 correlated to the diffusion of copper ions into the mixed oxides. The most notable change of
395 the CuO crystallites size is occurring within the MCAT-600 catalyst. In this case, before the
396 catalytic test, no CuO could be detected in XRD, while after the catalytic test, which can be
397 found in the supplementary information, the XRD analysis indicates the presence of CuO
398 crystals with sizes of around 18 nm. This may be due to the transformation of $Cu_{1.5}Mn_{1.5}O_4$
399 phase into a $CuMn_2O_4$ type phase as it was indicated evidenced by XRD analysis (Supplementary
400 figure 26). Part of the Cu^{2+} segregates from the structure and agglomerates as CuO.

401 The profiles of the CO conversion as a function of temperature under all the different
402 conditions indicate that the ZCAT-600, which has the largest CuO crystallite size, always
403 achieves the highest T_{50}. C/ZA-600 and C/ZAT-600 perform very similar which can be assigned
404 to the fact that these contain similar loadings of CuO with sizes in the same range. Only in the
405 lean and second stoichiometric cycle, C/ZA-600 shows a relatively higher T_{50} than C/ZAT-600.
406 At the same time, ZCA-600 reaches a lower T_{50} in the first stoichiometric cycle than C/ZAT-
407 600, again related to the smaller CuO size. However, in the second stoichiometric cycle, it
408 performs very comparable to C/ZAT-600, likely due to the growth of CuO crystallites. CO
409 oxidation at lower temperatures due to smaller or more disperse CuO particles has been
410 reported before. Higher CuO loading is also advantageous for CO conversion but only if good
411 dispersion can be assured(Luo et al., 2005; Xin et al., 2016). By using the LDH memory effect
412 both a high loading and good dispersion was ensured in C/ZAT-600 compared to ZCAT-600.

413 The Mn containing materials are generally superior for the CO conversion than those without.
414 C/MA-600 has in every case the lowest T_{50}, while MCAT-600 has most of the times the highest
415 T_{50}. Again, MCAT-600 has a much higher copper content and after the test it aggregates into

large CuO crystallites, explaining the higher T_{50}. The remarkable performance of the Cu-Mn compounds for CO oxidation is known since the first World War (1920), when mixtures of CuO and MnO_2 , known as hopcalite, were studied to be used in gas masks to prevent CO poisoning (Lamb et al., 1920; Almquist and Bray, 1923; Bliss, 1955). The difference between the materials used for gas masks and the materials in this application (three-way catalysis) is that the gas masks need to operate around room temperature, while for three-way catalysis it operates for long periods at high temperatures. In the case of three-way catalysis, the materials are already calcined at 600°C, so the crystallisation of the compounds explains why they are unable to convert CO at room temperature. For MCAT-600, the copper manganite structure is more crystalline than the other compounds, which can also explain the higher T_{50} for CO. A possible reason for the best performance of C/MA-600 for CO conversion is related to the amorphous alumina present, which helps disperse the Cu and Mn mixtures over the entire material, inhibiting their agglomeration and further crystallization. Furthermore, the higher surface area of C/MA-600 as compared to C/MT-600 and C/MZAT-600 also contributes to better dispersion. Moreover, the propene/propane conversion profiles and the benchmarking of the catalyst are discussed in detail in the Supplementary Information. A further discussion on the mechanisms that take place on CuO and copper manganite can be found in the literature (Cocke and Vepřek, 1986; Vepřek et al., 1986; Buciuman et al., 1999; Van Everbroeck et al., 2020).

The formation of N_2O and NH_3 can occur from NO reduction, as reaction intermediates (Jobson et al., 1994; Okamoto and Gotoh, 1997; Okamoto et al., 1997; Granger et al., 2004; Nevalainen et al., 2018). In the current experiments, no N_2O is detected at low temperatures in stoichiometric and lean conditions, while in rich conditions, small quantities (< 20 ppm) of N_2O are sometimes detected above 400°C. Overall, the selectivity towards N_2O is very low. A

440 further discussion is on the NO conversion and selectivity is presented in the Supplementary
441 Information. Furthermore, corresponding stoichiometric, lean and rich conditions results as
442 well as reaction rates taking into account (i) specific surface area (Supplementary Figure 16,
443 17 and 18) and the (ii) amount of reactive sites of the catalyst (Supplementary Figure 19, 20
444 and 21) are detailed in the Supplementary Information.

445 To demonstrate the stability of the materials a structural investigation of the spent catalysts
446 is also presented in the Supplementary Information.

447 Conclusions

448 Layered double hydroxides with various compositions were prepared to obtain copper oxide
449 containing three-way catalysts. The Cu source was added following two different methods, (a)
450 during the LDH synthesis via co-precipitation and (b) by reconstruction of the calcined LDOs
451 material based on the unique memory effect property. Larger amounts of CuO nanoparticles
452 can be loaded on the three-way catalysts by using the reconstruction method, but a well-
453 crystallized starting LDH structure is necessary for an effective reconstruction process.

454 Catalytic testing of the obtained three-way catalysts showed that the CO and the
455 hydrocarbons, e. g. propene and propane, were generally converted at lower temperatures
456 when CuO crystallites were smaller and well-dispersed. A synergistic effect was observed
457 when Mn atoms were present in the catalysts structure. Further, it was demonstrated that a
458 better dispersion of CuO was more important than achieving high loadings of CuO
459 nanoparticles on the three-way catalysts. The presence of Al in the LDH layers creates a more
460 appropriate support material, compared to the presence of Ti in the layers, due to the fact
461 that it enabled a higher Cu dispersion and provided a higher surface area. The main drawback
462 observed in the case of Ti-containing catalysts is directly related to its crystallisation to rutile,

after long exposure to high temperatures. However, the addition of Zn prevented the crystallisation of rutile by the formation of Zn_2TiO_4, which was advantageous for the propene conversion process. On the other hand, the presence of Ti proved to be beneficial for the conversion and the selectivity towards N_2 in the NO conversion. Highly dispersed CuO on the supporting material was again one of the most important factors to reach a high catalyst activity. These conclusions offer new insights in the design of LDH-based MMOs for the reduction of CRMs in three-way catalytic convertors.

Acknowledgements

The authors acknowledge financial support by the European Union's Horizon 2020 Project Partial-PGMs (H2020-NMP-686086). R-G C. and P.C. acknowledge the FWO-Flanders (project no. G038215N) for financial support. S.B and D.A.E thank the financial support of the European Research Council (ERC-CoG-2019 815128). The authors are grateful to Johnson Matthey, UK, for supplying the commercial benchmark catalysts.

Bibliography

Aisawa, S., Hirahara, H., Uchiyama, H., Takahashi, S., Narita, E., 2002. Synthesis and Thermal Decomposition of Mn–Al Layered Double Hydroxides. J. Solid State Chem. 167, 152–159. https://doi.org/https://doi.org/10.1006/jssc.2002.9637

Almquist, J.A., Bray, W.C., 1923. The Catalytic Oxidation of Carbon Monoxide. I. Efficiency of the Catalysts, Manganese Dioxide, Cupric Oxide and Mixtures of These Oxides. J. Am. Chem. Soc. 45, 2305–2322. https://doi.org/10.1021/ja01663a011

Behar, S., Gonzalez, P., Agulhon, P., Quignard, F., Świerczyński, D., 2012. New synthesis of nanosized Cu–Mn spinels as efficient oxidation catalysts. Catal. Today 189, 35–41. https://doi.org/10.1016/J.CATTOD.2012.04.004

Bennici, S., Carniti, P., Gervasini, A., 2004. Bulk and Surface Properties of Dispersed CuO Phases in Relation with Activity of NOxReduction. Catal. Letters 98, 187–194. https://doi.org/10.1007/s10562-004-8679-9

Biasin, A., Fabro, J., Michelon, N., Glisenti, A., Canu, P., 2019. Investigation of thermal effects on heterogeneous exothermic reactions and their impact on kinetics studies. Chem. Eng. J. https://doi.org/10.1016/j.cej.2018.10.116

Biemelt, T., Wegner, K., Teichert, J., Lohe, M.R., Martin, J., Grothe, J., Kaskel, S., 2016. Hopcalite nanoparticle catalysts with high water vapour stability for catalytic oxidation of carbon monoxide. Appl. Catal. B Environ. 184, 208–215. https://doi.org/10.1016/J.APCATB.2015.11.008

Blasse, G., 1966. Ferromagnetism and ferrimagnetism of oxygen spinels containing tetravalent manganese. J. Phys. Chem. Solids 27, 383–389. https://doi.org/10.1016/0022-3697(66)90045-X

Bliss, A., 1955. Arthur Becket Lamb February 25,1880 - May 15, 1952. J. Am. Chem. Soc. 77, 5773–5780. https://doi.org/10.1021/ja01627a600

Buciuman, F.C., Patcas, F., Hahn, T., 1999. A spillover approach to oxidation catalysis over copper and manganese mixed oxides. Chem. Eng. Process. Process Intensif. 38, 563–569. https://doi.org/10.1016/S0255-2701(99)00053-7

Carja, G., Dartu, L., Okada, K., Fortunato, E., 2013. Nanoparticles of copper oxide on layered double hydroxides and the derived solid solutions as wide spectrum active nano-photocatalysts. Chem. Eng. J. 222, 60–66. https://doi.org/10.1016/j.cej.2013.02.039

Carja, G., Kameshima, Y., Ciobanu, G., Okada, K., 2010. Oleate-LDH hybrids by the successive use of the clay structural “memory effect,” in: Journal of Nanoscience and Nanotechnology. https://doi.org/10.1166/jnn.2010.1389

Cavani, F., Trifiro, F., Vaccari, A., 1991. Hydrotalcite-type anionic clays: Preparation, properties and applications. Catal. Today 11, 173–301. https://doi.org/10.1016/0920-5861(91)80068-K

510 Chen, L., Si, Z., Wu, X., Weng, D., 2014. DRIFT Study of CuO–CeO2–TiO2 Mixed Oxides for NOx
511 Reduction with NH3 at Low Temperatures. ACS Appl. Mater. Interfaces 6, 8134–8145.
512 https://doi.org/10.1021/am5004969

513 Choukroun, D., Daems, N., Kenis, T., Van Everbroeck, T., Hereijgers, J., Altantzis, T., Bals, S., Cool, P.,
514 Breugelmans, T., 2020. Bifunctional Nickel–Nitrogen-Doped-Carbon-Supported Copper
515 Electrocatalyst for CO2 Reduction. J. Phys. Chem. C 124, 1369–1381.
516 https://doi.org/10.1021/acs.jpcc.9b08931

517 Clarke, T.J., Davies, T.E., Kondrat, S.A., Taylor, S.H., 2015. Mechanochemical synthesis of copper
518 manganese oxide for the ambient temperature oxidation of carbon monoxide. Appl. Catal. B
519 Environ. https://doi.org/10.1016/j.apcatb.2014.09.070

520 Cocke, D.L., Vepřek, S., 1986. First direct evidence of a solid state charge transfer redox system Cu+2
521 + Mn3+ ⇋ Cu1+ + Mn4+in copper manganese oxide. Solid State Commun. 57, 745–748.
522 https://doi.org/10.1016/0038-1098(86)90851-3

523 Cousin, P., Ross, R.A., 1990. Preparation of mixed oxides: a review. Mater. Sci. Eng. A 130, 119–125.
524 https://doi.org/10.1016/0921-5093(90)90087-J

525 Erickson, K.L., Bostrom, T.E., Frost, R.L., 2005. A study of structural memory effects in synthetic
526 hydrotalcites using environmental SEM. Mater. Lett. 59, 226–229.
527 https://doi.org/https://doi.org/10.1016/j.matlet.2004.08.035

528 European Automobile Manufacturers Association, 2021. Fuel types of new cars: electric 10.5%,
529 hybrid 11.9%, petrol 47.5% market share full-year 2020 [WWW Document]. 4/2/2021. URL
530 https://www.acea.auto/fuel-pc/fuel-types-of-new-cars-electric-10-5-hybrid-11-9-petrol-47-5-
531 market-share-full-year-2020/ (accessed 11.11.21).

532 European Commission, 2018. Report on Critical Raw Materials and the Circular Economy Part 1/3,
533 Commission staff working document. https://doi.org/10.1097/PPO.0b013e3181b9c5d5

534 Fridrichová, J., Bacik, P., Ertl, A., Wildner, M., Dekan, J., Miglierini, M., 2017. Jahn-Teller distortion of
535 Mn 3+ -occupied octahedra in red beryl from Utah indicated by optical spectroscopy. J. Mol.
536 Struct. 1152. https://doi.org/10.1016/j.molstruc.2017.09.081

537 Friedman, R.M., Freeman, J.J., Lytle, F.W., 1978. Characterization of CuAl2O3 catalysts. J. Catal. 55,
538 10–28. https://doi.org/https://doi.org/10.1016/0021-9517(78)90181-1

539 Gates-Rector, S., Blanton, T., 2019. The Powder Diffraction File: a quality materials characterization
540 database. Powder Diffr. 34, 352–360. https://doi.org/DOI: 10.1017/S0885715619000812

541 Gennequin, C., Barakat, T., Tidahy, H.L., Cousin, R., Lamonier, J.-F., Aboukaïs, A., Siffert, S., 2010. Use
542 and observation of the hydrotalcite “memory effect” for VOC oxidation. Catal. Today 157, 191–
543 197. https://doi.org/https://doi.org/10.1016/j.cattod.2010.03.012

544 Gong, J., Liu, T., Wang, X., Hu, X., Zhang, L., 2011. Efficient Removal of Heavy Metal Ions from
545 Aqueous Systems with the Assembly of Anisotropic Layered Double Hydroxide
546 Nanocrystals@Carbon Nanosphere. Environ. Sci. Technol. 45, 6181–6187.
547 https://doi.org/10.1021/es200668q

548 Granger, P., Malfoy, P., Leclercq, G., 2004. Kinetics of the CO+N2O reaction over noble metals: II.
549 Rh/Al2O3 and Pt–Rh/Al2O3. J. Catal. 223, 142–151.
550 https://doi.org/https://doi.org/10.1016/j.jcat.2004.01.017

551 Hargreaves, J.S.J., 2016. Some considerations related to the use of the Scherrer equation in powder
552 X-ray diffraction as applied to heterogeneous catalysts. Catal. Struct. React. 2, 33–37.
553 https://doi.org/10.1080/2055074X.2016.1252548

554 Iwamoto, M., Yahiro, H., 2003. Zeolites in the Science and Technology of Nitrogen Monoxide
555 Removal. https://doi.org/10.1201/9780203911167.ch19

556 Jahn, H.A., Teller, E., Donnan, F.G., 1937. Stability of polyatomic molecules in degenerate electronic
557 states - I—Orbital degeneracy. Proc. R. Soc. London. Ser. A - Math. Phys. Sci. 161, 220–235.

https://doi.org/10.1098/rspa.1937.0142

Jobson, E., Smedler, G., Malmberg, P., Bernler, H., Hjortsberg, O., Gottberg, I., Rosén, Å., 1994. Nitrous Oxide Formation Over Three-Way Catalyst. SAE Trans. 103, 519–530.

Kašpar, J., Fornasiero, P., Hickey, N., 2003. Automotive catalytic converters: current status and some perspectives. Catal. Today 77, 419–449. https://doi.org/https://doi.org/10.1016/S0920-5861(02)00384-X

Kowalik, P., Konkol, M., Kondracka, M., Próchniak, W., Bicki, R., Wiercioch, P., 2013. Memory effect of the CuZnAl-LDH derived catalyst precursor—In situ XRD studies. Appl. Catal. A Gen. 464–465, 339–347. https://doi.org/https://doi.org/10.1016/j.apcata.2013.05.048

Kumar, K., Kumar, N., Singh, H., 2017. Comprehensive Review of Three way Catalytic Converter 3, 1188–1196.

Kummer, J.T., 1980. Catalysts for automobile emission control. Prog. Energy Combust. Sci. 6, 177–199. https://doi.org/10.1016/0360-1285(80)90006-4

Lamb, A.B., Bray, W.C., Frazer, J.C.W., 1920. The Removal of Carbon Monoxide from Air. J. Ind. Eng. Chem. 12, 213–221. https://doi.org/10.1021/ie50123a007

Larsson, P.-O., Andersson, A., 1998. Complete Oxidation of CO, Ethanol, and Ethyl Acetate over Copper Oxide Supported on Titania and Ceria Modified Titania. J. Catal. 179, 72–89. https://doi.org/10.1006/JCAT.1998.2198

Larsson, P.O., Andersson, A., Wallenberg, L.R., Svensson, B., 1996. Combustion of CO and toluene; characterisation of copper oxide supported on titania and activity comparisons with supported cobalt, iron, and manganese oxide. J. Catal. https://doi.org/10.1006/jcat.1996.0329

Li, Q., Meng, M., Dai, F., Zha, Y., Xie, Y., Hu, T., Zhang, J., 2012. Multifunctional hydrotalcite-derived K/MnMgAlO catalysts used for soot combustion, NOx storage and simultaneous soot–NOx

581 removal. Chem. Eng. J. 184, 106–112.
582 https://doi.org/http://dx.doi.org/10.1016/j.cej.2012.01.009

583 Li, Q., Meng, M., Xian, H., Tsubaki, N., Li, X., Xie, Y., Hu, T., Zhang, J., 2010. Hydrotalcite-Derived
584 MnxMg3−xAlO Catalysts Used for Soot Combustion, NOx Storage and Simultaneous Soot-NOx
585 Removal. Environ. Sci. Technol. 44, 4747–4752. https://doi.org/10.1021/es9033638

586 LI, Q., WANG, X., CHANG, W., CHEN, H., ZHANG, Z., 2014. Promotional effects of cerium doping and
587 NOx on the catalytic soot combustion over MnMgAlO hydrotalcite-based mixed oxides. J. Rare
588 Earths 32, 176–183. https://doi.org/https://doi.org/10.1016/S1002-0721(14)60048-X

589 Li, Y., Tang, L., Ma, X., Wang, X., Zhou, W., Bai, D., 2017. Synthesis and characterization of Zn-Ti
590 layered double hydroxide intercalated with cinnamic acid for cosmetic application. J. Phys.
591 Chem. Solids 107, 62–67. https://doi.org/10.1016/j.jpcs.2017.02.018

592 Liang, X., Zang, Y., Xu, Y., Tan, X., Hou, W., Wang, L., Sun, Y., 2013. Sorption of metal cations on
593 layered double hydroxides. Colloids Surfaces A Physicochem. Eng. Asp. 433, 122–131.
594 https://doi.org/https://doi.org/10.1016/j.colsurfa.2013.05.006

595 Liu, C., Zhang, Z., Zhai, X., Wang, X., Gui, J., Zhang, C., Zhu, Y., Li, Y., 2019. Synergistic effect between
596 copper and different metal oxides in the selective hydrogenolysis of glucose. New J. Chem. 43,
597 3733–3742. https://doi.org/10.1039/C8NJ05815F

598 Luo, M.-F., Fang, P., He, M., Xie, Y.-L., 2005. In situ XRD, Raman, and TPR studies of CuO/Al2O3
599 catalysts for CO oxidation. J. Mol. Catal. A Chem. 239, 243–248.
600 https://doi.org/https://doi.org/10.1016/j.molcata.2005.06.029

601 Marchi, A.J., Apesteguía, C.R., 1998. Impregnation-induced memory effect of thermally activated
602 layered double hydroxides. Appl. Clay Sci. 13, 35–48.
603 https://doi.org/https://doi.org/10.1016/S0169-1317(98)00011-8

604 Mejía-Centeno, I., Castillo, S., Fuentes, G.A., 2012. Enhanced emissions of NH3, N2O and H2 from a

605 Pd-only TWC and supported Pd model catalysts: Light-off and sulfur level studies. Appl. Catal. B
606 Environ. 119–120, 234–240. https://doi.org/https://doi.org/10.1016/j.apcatb.2012.02.030

607 Mista, W., Zawadzki, M., Grabowska, H., 2003. Hydrothermal preparation of CuO-ZnAl2O4 catalyst
608 for phenol ortho-alkylation with methanol: effect of the calcination temperature on the
609 catalytic performance. Res. Chem. Intermed. 29, 137–146.
610 https://doi.org/10.1163/156856703321505030

611 Mrad, R., Cousin, R., Saliba, N.A., Tidahy, L., Siffert, S., 2015. Degradation of VOCs and NOx over
612 Mg(Cu)–AlFe mixed oxides derived from hydrotalcite-like compounds. Comptes Rendus Chim.
613 18, 351–357. https://doi.org/http://dx.doi.org/10.1016/j.crci.2014.08.005

614 Nevalainen, P., Kinnunen, N.M., Kirveslahti, A., Kallinen, K., Maunula, T., Keenan, M., Suvanto, M.,
615 2018. Formation of NH3 and N2O in a modern natural gas three-way catalyst designed for
616 heavy-duty vehicles: the effects of simulated exhaust gas composition and ageing. Appl. Catal. A
617 Gen. 552, 30–37. https://doi.org/https://doi.org/10.1016/j.apcata.2017.12.017

618 Obalová, L., Karásková, K., Jirátová, K., Kovanda, F., 2009. Effect of potassium in calcined Co–Mn–Al
619 layered double hydroxide on the catalytic decomposition of N2O. Appl. Catal. B Environ. 90,
620 132–140. https://doi.org/http://dx.doi.org/10.1016/j.apcatb.2009.03.002

621 Obalová, L., Pacultová, K., Balabánová, J., Jirátová, K., Bastl, Z., Valášková, M., Lacný, Z., Kovanda, F.,
622 2007. Effect of Mn/Al ratio in Co-Mn-Al mixed oxide catalysts prepared from hydrotalcite-like
623 precursors on catalytic decomposition of N2O. Catal. Today.
624 https://doi.org/10.1016/j.cattod.2006.08.027

625 Okamoto, Y., Gotoh, H., 1997. Copper-zirconia catalysts for NO□CO reactions. Catal. Today 36, 71–79.
626 https://doi.org/10.1016/S0920-5861(96)00198-8

627 Okamoto, Y., Gotoh, H., Hishida, K., Aritani, H., Tanaka, T., Yoshida, S., 1997. Surface copper-TiO2
628 interaction species for NO□CO reactions. Appl. Surf. Sci. 121–122, 509–512.

https://doi.org/10.1016/S0169-4332(97)00355-3

Pacultová, K., Karásková, K., Kovanda, F., Jirátová, K., Šrámek, J., Kustrowski, P., Kotarba, A., Chromčáková, Ž., Kočí, K., Obalová, L., 2016. K-Doped Co–Mn–Al Mixed Oxide Catalyst for N2O Abatement from Nitric Acid Plant Waste Gases: Pilot Plant Studies. Ind. Eng. Chem. Res. 55, 7076–7084. https://doi.org/10.1021/acs.iecr.6b01206

Patel, A., Shukla, P., Chen, J., Rufford, T.E., Wang, S., Rudolph, V., Zhu, Z., 2015. Structural sensitivity of mesoporous alumina for copper catalyst loading used for NO reduction in presence of CO. Chem. Eng. Res. Des. 101, 27–43. https://doi.org/10.1016/J.CHERD.2015.03.027

Patel, A., Shukla, P., Pan, G.T., Chong, S., Rudolph, V., Zhu, Z., 2017. Influence of copper loading on mesoporous alumina for catalytic NO reduction in the presence of CO. J. Environ. Chem. Eng. 5, 2350–2361. https://doi.org/10.1016/J.JECE.2017.04.035

Pérez, M.R., Pavlovic, I., Barriga, C., Cornejo, J., Hermosín, M.C., Ulibarri, M.A., 2006. Uptake of Cu2+, Cd2+ and Pb2+ on Zn–Al layered double hydroxide intercalated with edta. Appl. Clay Sci. 32, 245–251. https://doi.org/https://doi.org/10.1016/j.clay.2006.01.008

Prevot, V., Briois, V., Cellier, J., Forano, C., Leroux, F., 2008. An in-situ investigation of LDH–acetate prepared in polyol, under moderate thermal treatment. J. Phys. Chem. Solids 69, 1091–1094. https://doi.org/https://doi.org/10.1016/j.jpcs.2007.10.051

Reichle, W.T., Kang, S.Y., Everhardt, D.S., 1986. The nature of the thermal decomposition of a catalytically active anionic clay mineral. J. Catal. 101, 352–359. https://doi.org/https://doi.org/10.1016/0021-9517(86)90262-9

Richardson, M.C., Braterman, P.S., 2009. Cation exchange by anion-exchanging clays: the effects of particle aging. J. Mater. Chem. 19, 7965–7975. https://doi.org/10.1039/B908516E

Ruiz Puigdollers, A., Schlexer, P., Tosoni, S., Pacchioni, G., 2017. Increasing Oxide Reducibility: The Role of Metal/Oxide Interfaces in the Formation of Oxygen Vacancies. ACS Catal. 7, 6493–6513.

https://doi.org/10.1021/acscatal.7b01913

Saber, O., Tagaya, H., 2008. Preparation and intercalation reactions of nano-structural materials, Zn-Al-Ti LDH. Mater. Chem. Phys. https://doi.org/10.1016/j.matchemphys.2007.10.024

Saber, O., Tagaya, H., 2003. New Layered Double Hydroxide, Zn-Ti LDH: Preparation and Intercalation Reactions. J. Incl. Phenom. 45, 109–116.

Saber, O., Zaki, T., 2014. Carbon monoxide oxidation using Zn--Cu--Ti hydrotalcite-derived catalysts. J. Chem. Sci. 126, 981–988. https://doi.org/10.1007/s12039-014-0642-8

Schön, A., Dacquin, J.-P., Dujardin, C., Granger, P., 2017. Catalytic Activity and Thermal Stability of LaFe1−xCuxO3 and La2CuO4 Perovskite Solids in Three-Way-Catalysis. Top. Catal. 60, 300–306. https://doi.org/10.1007/s11244-016-0615-x

Schön, A., Dacquin, J.-P., Granger, P., Dujardin, C., 2018. Non stoichiometric La1-yFeO3 perovskite-based catalysts as alternative to commercial three-way-catalysts? – Impact of Cu and Rh doping. Appl. Catal. B Environ. 223, 167–176. https://doi.org/https://doi.org/10.1016/j.apcatb.2017.06.026

Schön, A., Dujardin, C., Dacquin, J.-P., Granger, P., 2015. Enhancing catalytic activity of perovskite-based catalysts in three-way catalysis by surface composition optimisation. Catal. Today 258, 543–548. https://doi.org/https://doi.org/10.1016/j.cattod.2014.11.002

Seftel, E., Popovici, E., Mertens, M., Witte, K. De, Tendeloo, G. Van, Cool, P., Vansant, E.F., 2008. Zn–Al layered double hydroxides: Synthesis, characterization and photocatalytic application. Microporous Mesoporous Mater. 113, 296–304. https://doi.org/https://doi.org/10.1016/j.micromeso.2007.11.029

Seftel, E.M., Ciocarlan, R.G., Michielsen, B., Meynen, V., Mullens, S., Cool, P., 2018. Insights into phosphate adsorption behavior on structurally modified ZnAl layered double hydroxides. Appl. Clay Sci. 165, 234–246. https://doi.org/https://doi.org/10.1016/j.clay.2018.08.018

677 Seftel, E.M., Popovici, E., Mertens, M., Van Tendeloo, G., Cool, P., Vansant, E.F., 2008. The influence
678 of the cationic ratio on the incorporation of Ti4+ in the brucite-like sheets of layered double
679 hydroxides. Microporous Mesoporous Mater. 111, 12–17.
680 https://doi.org/10.1016/j.micromeso.2007.07.008

681 Severino, F., Brito, J.L., Laine, J., Fierro, J.L.G., Agudo, A.L., 1998. Nature of Copper Active Sites in the
682 Carbon Monoxide Oxidation on CuAl2O4and CuCr2O4Spinel Type Catalysts. J. Catal. 177, 82–95.
683 https://doi.org/10.1006/JCAT.1998.2094

684 Stanimirova, T., Balek, V., 2008. Characterization of Mg-Al-CO3 Layered Double Hydroxides prepared
685 by re-hydration of Mg-Al mixed oxide. J. Therm. Anal. Calorim. 94, 477–481.

686 Van Der Grift, C.J.G., Mulder, A., Geus, J.W., 1990. Characterization of silica-supported copper
687 catalysts by means of temperature-programmed reduction. Appl. Catal. 60, 181–192.
688 https://doi.org/10.1016/S0166-9834(00)82181-8

689 Van Everbroeck, T., Ciocarlan, R.-G., Hoey, W. Van, Mertens, M., Cool, P., 2020. Copper-Containing
690 Mixed Metal Oxides (Al, Fe, Mn) for Application in Three-Way Catalysis. Catalysts 10, 1344.
691 https://doi.org/10.3390/catal10111344

692 Vandenberghe, R.E., Legrand, E., Scheerlinck, D., Brabers, V.A.M., 1976. Neutron diffraction study of
693 the cation ordering in Cu1.5Mn1.5O4 and CuMg0.5Mn1.5O4. Acta Crystallogr. Sect. B 32, 2796–
694 2798. https://doi.org/10.1107/S056774087600890X

695 Vandenberghe, R.E., Robbrecht, G.G., Brabers, V.A.M., 1973. On the stability of the cubic spinel
696 structure in the system Cu□Mn□O. Mater. Res. Bull. 8, 571–579. https://doi.org/10.1016/0025-
697 5408(73)90134-7

698 Vepřek, S., Cocke, D.L., Kehl, S., Oswald, H.R., 1986. Mechanism of the deactivation of Hopcalite
699 catalysts studied by XPS, ISS, and other techniques. J. Catal. 100, 250–263.
700 https://doi.org/10.1016/0021-9517(86)90090-4

Wang, J., Chen, H., Hu, Z., Yao, M., Li, Y., 2015. A Review on the Pd-Based Three-Way Catalyst. Catal. Rev. 57, 79–144. https://doi.org/10.1080/01614940.2014.977059

Weng, L.T., Delmon, B., 1992. Phase cooperation and remote control effects in selective oxidation catalysts. Appl. Catal. A, Gen. https://doi.org/10.1016/0926-860X(92)80093-R

Wu, J., Dacquin, J.P., Cordier, C., Dujardin, C., Granger, P., 2019. Optimization of the Composition of Perovskite Type Materials for Further Elaboration of Four-Way Catalysts for Gasoline Engine. Top. Catal. 62, 368–375. https://doi.org/10.1007/s11244-018-1083-2

Xin, Q., Papavasilou, A., Boukos, N., Glisenti, A., Li, J.P.H., Yang, Y., Philippopoulos, C.J., Poulakis, E., Katsaros, F.K., Meynen, V., Cool, P., 2016. Preparation of CuO/SBA-15 catalyst by the modified ammonia driven deposition precipitation method with a high thermal stability and an efficient automotive CO and hydrocarbons conversion. Appl. Catal. B Environ. https://doi.org/10.1016/j.apcatb.2017.03.071

Yuan, D., Li, X., Zhao, Q., 2013. Preparation and characterization of Ni-Ti-O mixed oxide for selective catalytic reduction of NO under lean-burn conditions. Chinese J. Catal. 34, 1449–1455. https://doi.org/http://dx.doi.org/10.1016/S1872-2067(12)60614-7

Yuan, D., Li, X., Zhao, Q., Zhao, J., Tadé, M., Liu, S., 2014. A novel CuTi-containing catalyst derived from hydrotalcite-like compounds for selective catalytic reduction of NO with C3H6 under lean-burn conditions. J. Catal. 309, 268–279. https://doi.org/10.1016/j.jcat.2013.09.010

Zhao, Q., Yan, Z., Chen, C., Chen, J., 2017. Spinels: Controlled Preparation, Oxygen Reduction/Evolution Reaction Application, and Beyond. Chem. Rev. 117, 10121–10211. https://doi.org/10.1021/acs.chemrev.7b00051

Supplementary information

Reagents

All chemicals were purchased from Sigma-Aldrich/Merck and used without any further purification. The used chemicals are: $Cu(NO_3)_2.3H_2O$ (99.0 wt%), $Zn(NO_3)_2.6H_2O$ (99 wt%), $Al(NO_3)_3.9H_2O$ (99 wt%), $TiCl_4$ 99.9 wt%), $MnCl_2$ (97.0 wt%), NaOH (98.5 wt%), Na_2CO_3 (99.95-100.05 wt%), Copper acetate (98 wt%).

Sherrer equation:

The average crystallite size was estimated using the Scherrer equation:

$$d = \frac{K\lambda}{\beta \cos(\theta)}$$

Where, d = crystallite size, λ = the wavelength of the X-ray source (0.15406 nm), β = the full width at half maximum of the chosen diffraction peak (2θ), ϑ = Bragg angle and K = the shape constant chosen as 0.9. Using this equation, the morphological effects and disorder to reflection widths were not taken into account, so the obtained values were merely used for relative comparison of the materials (Hargreaves, 2016).

Catalytic activity measurements

The experiment consisted of four consecutive heating (at 5°C/min) and cooling cycles between 110 and 550°C, in different conditions (stoichiometric, lean, rich), preceded by a pre-treatment at 600°C in air and under stoichiometric condition.

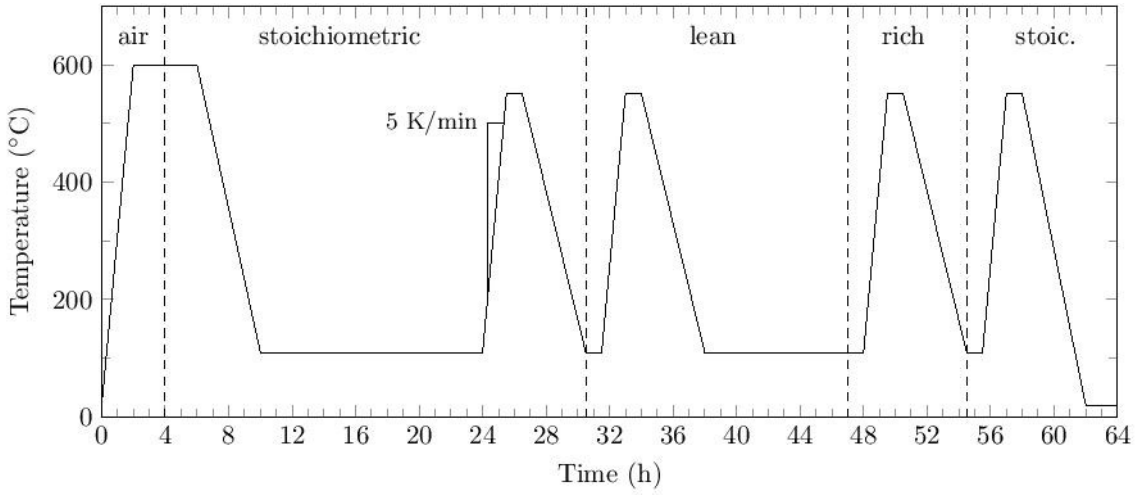

744

745 *Supplementary Figure 1: Procedure for catalytic testing.*

746 The gas composition for each of the conditions is described in Supplementary **¡Error! No se encuentra**
747 **el origen de la referencia.**. The flow rate was adjusted to correspond to a Gas Hourly Space Velocity of
748 60 000 mL h^{-1} g^{-1}. The composition of the gas at the outlet was monitored by a Thermo Scientific 42i-
749 HL chemiluminescence analyzer for NOx detection and an Agilent Technologies 490 micro GC for the
750 quantification of N_2, N_2O, H_2, CO, propane, propene and CO_2. The displayed conversions were
751 calculated from the heating cycles, using the following formula:

752 $$X_i(\%) = \left(1 - \frac{[i]}{[i]_0}\right) . 100$$

753 Where X_i = the conversion of compound *i*, *[i]* is the concentration of *i* at the outlet, and $[i]_0$ is the inlet
754 concentration of *i*.

755 The concentration of NH_3 was calculated using the following formula assuming that all NO not
756 converted to N_2 or N_2O leads to NH_3:

757 $$[NH_3] = [NO]_0 - ([NO] + 2\ [N_2] + 2\ [N_2O])$$

758 The selectivity of NO towards N_2 (S_{N_2}), N_2O (S_{N_2O}) and NH_3 (S_{NH_3}) were calculated as follows:

759 $$S_{N_2} = \frac{2\ [N_2]}{[NO]_0 - [NO]}$$

760 $$S_{N_2O} = \frac{2\ [N_2O]}{[NO]_0 - [NO]}$$

761 $$S_{NH_3} = \frac{[NH_3]}{[NO]_0 - [NO]}$$

762 The yield (Y_i) was determined as:

763 $$Y_i = X_i\ .S_i$$

764

Condition/Gas(vol%)	*NO*	*CO*	*C_3H_6*	*C_3H_8*	*H_2*	*O_2*	*CO_2*	*H_2O*	*He*
Stoichiometric	0.1	0.7	0.045	0.022	0.23	0.73	15	10	Balance
Lean	0.1	0.5	0.03	0.015	0.17	0.90	15	10	Balance
Rich	0.1	0.9	0.06	0.030	0.30	0.55	15	10	Balance

765 *Supplementary Table 3: Gas composition of the different conditions during the catalytic experiment.*

766

767 The specific reaction rate (Spec. RR) is calculated by dividing the reaction rate (RR) by the BET specific
768 surface area (SSA):

769 $$Spec.RR = \frac{RR}{SSA}$$

770 The reaction rate (RR) is calculated as follows (example for CO):

771 $$RR_{CO} = \frac{[CO]_0.X_{CO}.F.p}{T.R.g_{cat}}$$

772 *F* is the total flow rate, *p* the pressure (1.013 bar), *T* the temperature, *R* the gas constant. g_{cat} the
773 weight of the catalyst.

774 The turnover frequency is calculated by dividing the reaction rate (RR) by the number of moles Cu in
775 the catalyst, based on the SEM-EDX results:

776 $$TOF = \frac{RR}{\#\ mol\ CuO/g_{cat}}$$

777

778 ## Textural characteristics of the catalysts

779 The values for the BET specific surface area (SSA) of the different synthesized materials are
780 presented inSupplementary table 2. The evolution of the surface area through the different
781 synthesis steps can be deduced from left to right. Isotherms and additional textural properties
782 are presented in Supplementary figure 2 to 7. For the initial materials, the copper-containing
783 LDHs have each time a higher surface area than their non-copper containing LDHs (e. g. ZCA
784 vs. ZA or ZCAT vs. ZAT). At the same time, titanium and manganese presence in the materials
785 generally tends to increase the surface area (e. g. the case of ZAT, ZCAT, MZAT, MCAT or MT).
786 Comparing the three-way catalysts obtained by the thermal treatment at 600°C to the initial
787 ones, it can be concluded that the results are quite divergent; ZA, ZCA and MA increase their
788 surface area along with the synthesis steps, while the others decrease their surface area along
789 the process.

790

791

792

SSA (m^2/g)	Non-calcined	Calcined 400°C	Reconstructed	Three-way catalysts (calcined 600°C)
ZA	38	78	14	66
ZCA	45	-	-	63
ZAT	148	105	58	80
ZCAT	179	-	-	54

MZAT	195	130	113	46
MCAT	259	-	-	117
MA	66	188	98	73
MT	159	157	60	28

Supplementary table 2: BET specific surface area (SSA) of the synthesized materials in the different stages (non-calcined material, calcined at 400°C, after reconstruction in Cu-containing aqueous solutions and the obtained three-way catalysts produced by the calcination at 600°C).

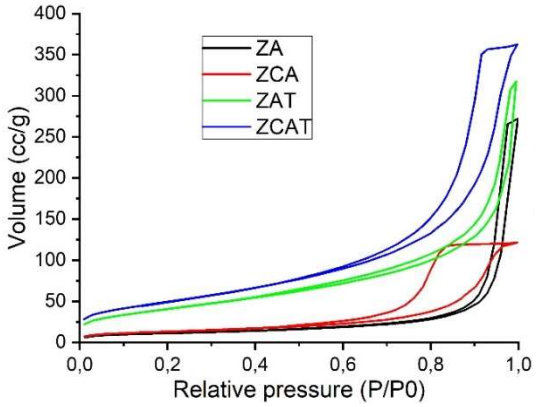

Supplementary figure 2: N_2-sorption isotherm of the materials prepared by co-precipitation (ZA, ZCA, ZAT, ZCAT).

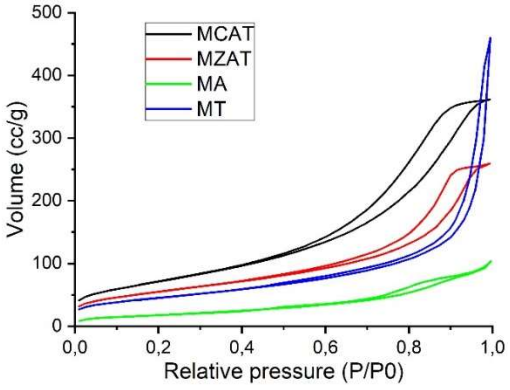

Supplementary figure 3: N_2-sorption isotherm of the materials prepared by co-precipitation (MCAT, MZAT, MA, MT).

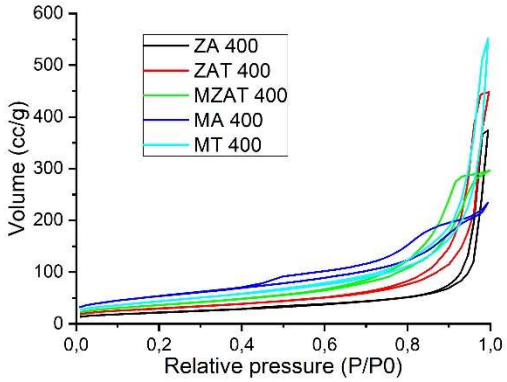

Supplementary figure 4: N_2-sorption isotherm of the materials calcined at 400 °C.

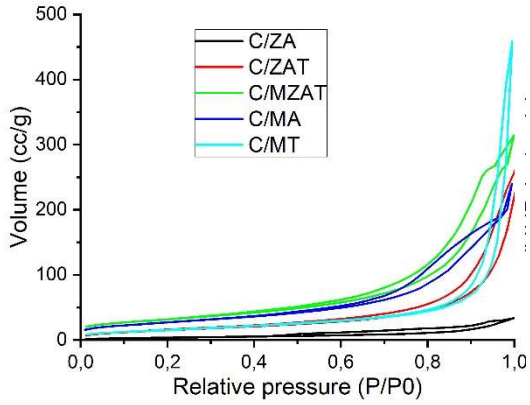

Supplementary figure 5: N_2-sorption isotherm of the materials after impregnation with Cu by the reconstruction method.

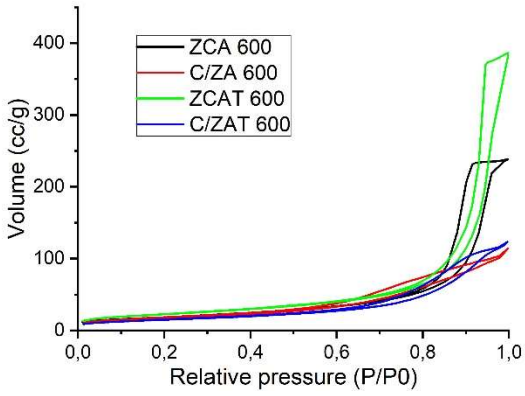

Supplementary figure 6: N_2-sorption isotherm of the final materials calcined at 600°C (ZCA 600, C/ZA 600, ZCAT 600, C/ZAT 600).

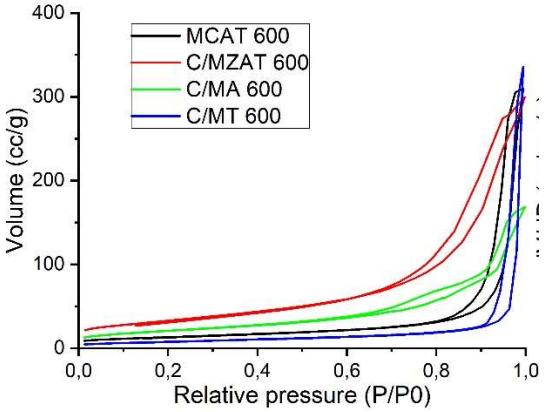

Supplementary figure 7: N_2-sorption isotherm of the final materials calcined at 600°C (MCAT 600, C/MZAT 600, C/MA 600, C/MT 600).

EDS mapping

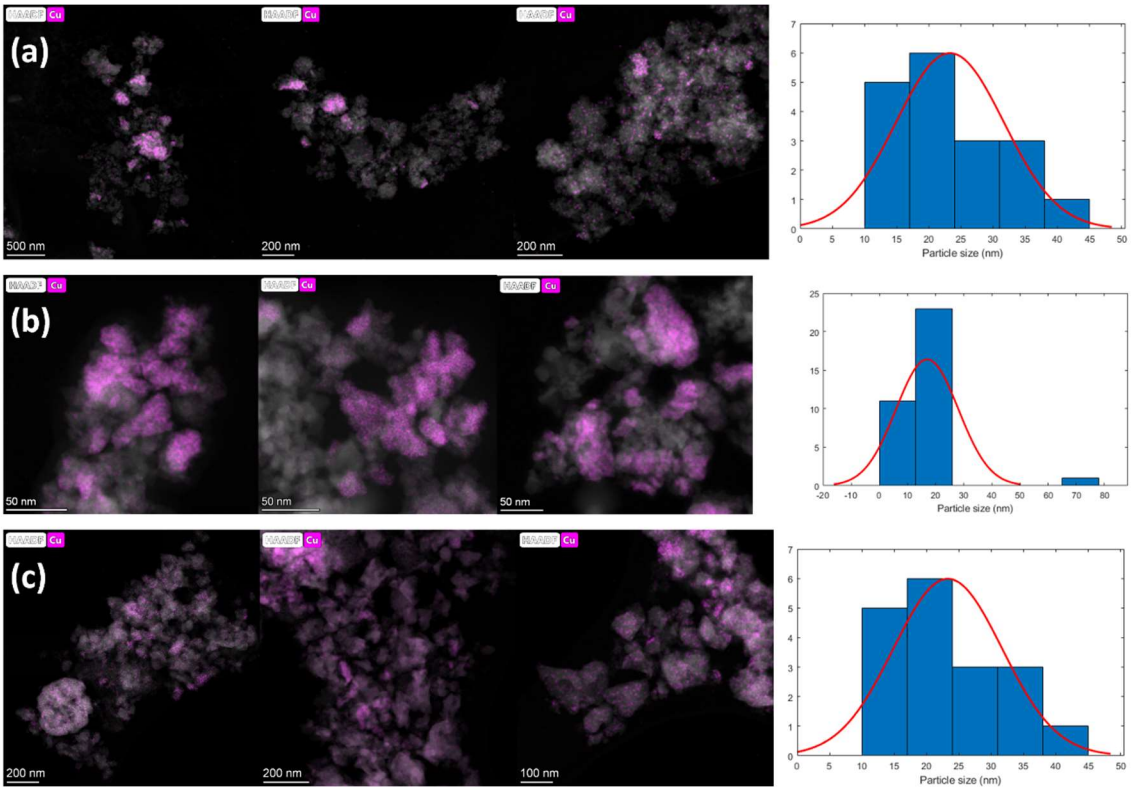

Supplementary figure 8: HAADF-STEM image with the EDS Cu mapping of different areas and CuO nanoparticles size distribution of (a) ZCAT-600, (b) C/ZAT-600 and (c) C/MA-600.

Catalytic activity testing

Stoic 1	Temperature 50 % conversion CO	C_3H_6	C_3H_8	max. NO conv.	temp. for max. NO conv.
ZCA-600	293	381	n.r.	1.2	327
C/ZA-600	329	436	n.r.	2.4	424
ZCAT-600	389	457	n.r.	4.9	453
C/ZAT-600	325	356	552	8	387
MCAT-600	314	534	577	2.4	576
C/MZAT-600	276	331	549	8.1	341
C/MA-600	239	409	497	11.7	522
C/MT-600	269	528	n.r.	9.5	429
Comm. TWC	217	262	454	47.1	285
0.5% Pd/$CeZrO_2$	136	177	532	27	232

Supplementary table 3: temperatures at which 50 % conversion is reached and maximal NO conversion in the first stoichiometric cycle. N.r. = not reached.

Under lean conditions (Supplementary Figure 9), one would expect lower NO conversions and higher conversions of CO and the organic compounds, due to the relatively higher amount of O_2 present. The maximal NO conversion is indeed lower (< 5%), except for C/MA-600, which still manages to convert up to 10.7%. CO and propene conversions are very comparable to the first stoichiometric cycle, while propane conversion is slightly improved.

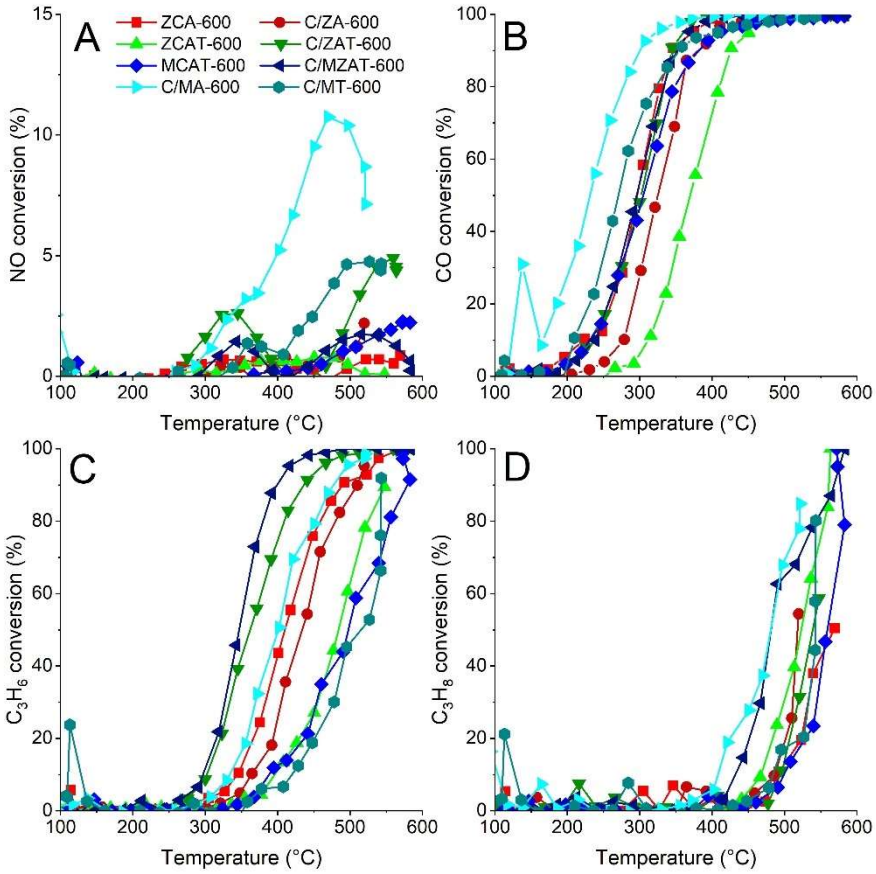

835

836 *Supplementary Figure 9: Temperature programmed conversion curves under lean conditions, A: NO conversion, B: CO*

837 *conversion, C: propene conversion, D: propane conversion.*

838

	Temperature 50% conversion			max. NO conv.	temp. for max. NO conv.
Lean	CO	C_3H_6	C_3H_8		
ZCA-600	297	410	568	0.9	569
C/ZA-600	325	434	518	2.2	520
ZCAT-600	370	484	539	0.8	451
C/ZAT-600	302	362	523	4.9	560

MCAT-600	311	525	570	2.3	573
C/MZAT-600	296	347	481	1.7	515
C/MA-600	231	401	481	10.7	470
C/MT-600	271	515	542	4.8	527
Comm. TWC	198	213	466	17.5	305
0.5% Pd/$CeZrO_2$	188	247	521	18	368

Supplementary Table 4: temperatures at which 50% conversion is reached and maximal NO conversion in the lean cycle. N.r. = not reached.

In the rich condition (Supplementary Figure 10), less O_2 is present so NO is more likely to oxidise CO and the hydrocarbons. This is clearly the case here, as NO conversion reaches nearly 100% in all the cases. C/MZAT-600 stands out with the lowest T_{50}, while ZCAT-600 and MCAT-600 perform considerably worse. The T_{50} for CO and propene are slightly higher, but the conversion of propane is definitely worse as none of the studied three-way catalysts are able to convert up to 50% propane under 550°C.

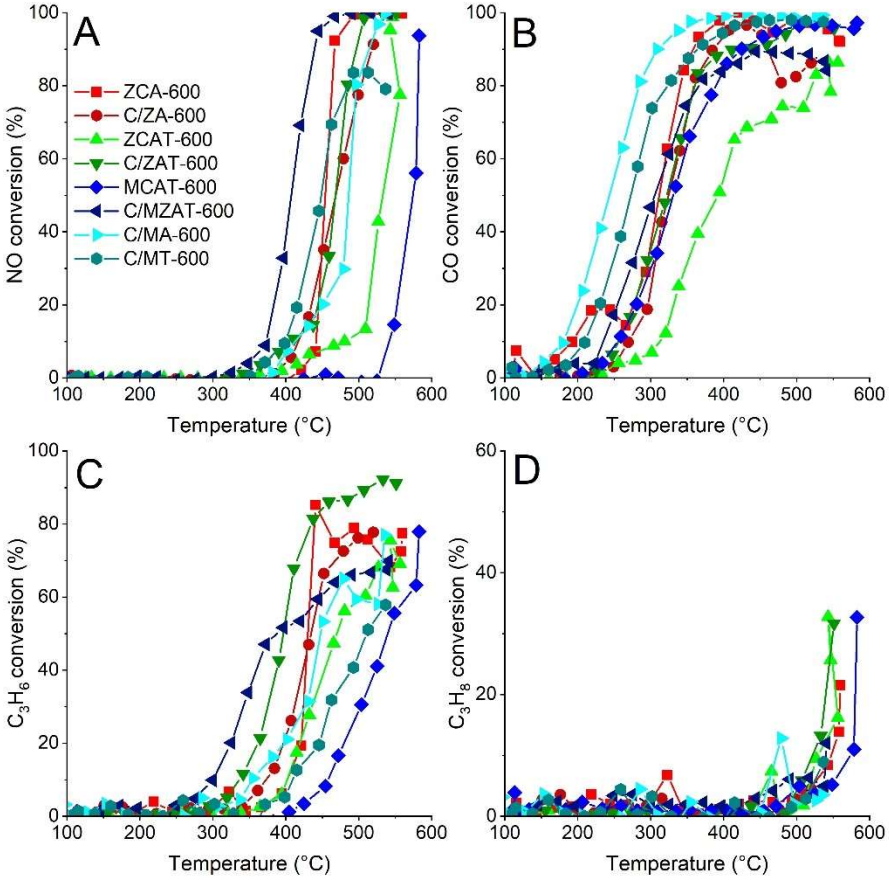

848

849 *Supplementary Figure 10: Temperature programmed conversion curves under rich conditions, A: NO conversion, B: CO*

850 *conversion, C: propene conversion, D: propane conversion.*

851

	Temperature 50% conversion			
Rich	CO	C_3H_6	C_3H_8	NO
ZCA-600	312	430	n.r.	454
C/ZA-600	325	435	n.r.	468
ZCAT-600	392	470	n.r.	533
C/ZAT-600	322	396	n.r.	468
MCAT-600	331	540	n.r.	574
C/MZAT-600	306	388	n.r.	407

C/MA-600	243	448	n.r.	486
C/MT-600	273	511	n.r.	449
Comm. TWC	240	333	441	286
0.5% Pd/$CeZrO_2$	137	352	456	136

Supplementary Table 54: temperatures at which 50% conversion is reached in the rich cycle. N.r. = not reached.

Propene and propane discussion

The general trend that a higher T_{50} is associated with the presence of larger CuO crystallite sizes is not observed from the propene conversion profiles. The addition of manganese in the three-way catalysts does not improve the propene conversion much. The three-way catalysts C/ZAT-600 and C/MZAT-600 perform the best, showing every time the lowest T_{50} and achieving more than 90% conversion at the lowest temperatures, while the lowest catalytic conversions are found with MCAT-600 and C/MT-600. C/MA-600 on the other hand performs better and its profile is even similar to C/MZAT-600 in the last stoichiometric cycle. This demonstrates again that using alumina certainly represents an advantage over titania, probably because it behaves better as a mesoporous support than titania which further crystallizes into a rutile structure during the catalytic tests. This assumption is also supported by the superior activity of the C/ZAT-600 and C/MZAT-600, in which the solid state reaction between the ZnO and TiO_2 leads to the formation of Zn_2TiO_4 thus inhibiting the crystallisation into a rutile phase.

Not much distinction can be made between the different three-way catalysts in the propane conversion profiles. Only C/MA-600 clearly shows the best performances compared to all the studied three-way catalysts, with its much lower T_{50}. Similarly as hypothesized for the CO and

propene conversion, this may be assigned to the presence of the amorphous alumina which inhibits agglomeration of the copper and manganese, while the surface area enhances their dispersion.

The purpose of the second stoichiometric cycle is to compare it with the first one, in order to check whether the performance of the catalysts is declining or not after this long dynamic procedure. For all the samples, except C/MA-600, the maximal NO conversion is lower, under 6%. Similar CO conversions as in the first catalytic cycle are observed. Surprisingly, some catalysts even have a lower T_{50} compared to the first catalytic cycle. For example, the T_{50} for MCAT-600 is 62°C lower than in the first cycle (314°C and 252°C). For the propene conversion the situation is the same. There is a difference of 114°C for MCAT-600 between the first and the second catalytic cycle (534°C and 420°C), while the propane conversion is very similar between the two catalytic cycles.

	Temperature 50% conversion			max. NO conv.	temp. for max. NO conv.
Stoic 2	CO	C_3H_6	C_3H_8		
ZCA-600	310	384	567	1.2	371
C/ZA-600	346	370	n.r.	5.8	395
ZCAT-600	390	459	n.r.	5.6	432
C/ZAT-600	301	332	561	4.2	348

MCAT-600	252	420	568	2	583
C/MZAT-600	274	353	524	1.4	332
C/MA-600	239	353	464	9.5	527
C/MT-600	255	452	n.r.	2.8	337
Comm. TWC	228	268	456	52	358
0.5% $Pd/CeZrO_2$	157	231	507	39	259

886 *Supplementary Table 6: Temperatures at which 50% conversion is reached and maximal NO conversion in the second*

887 *stoichiometric cycle N.r. = not reached.*

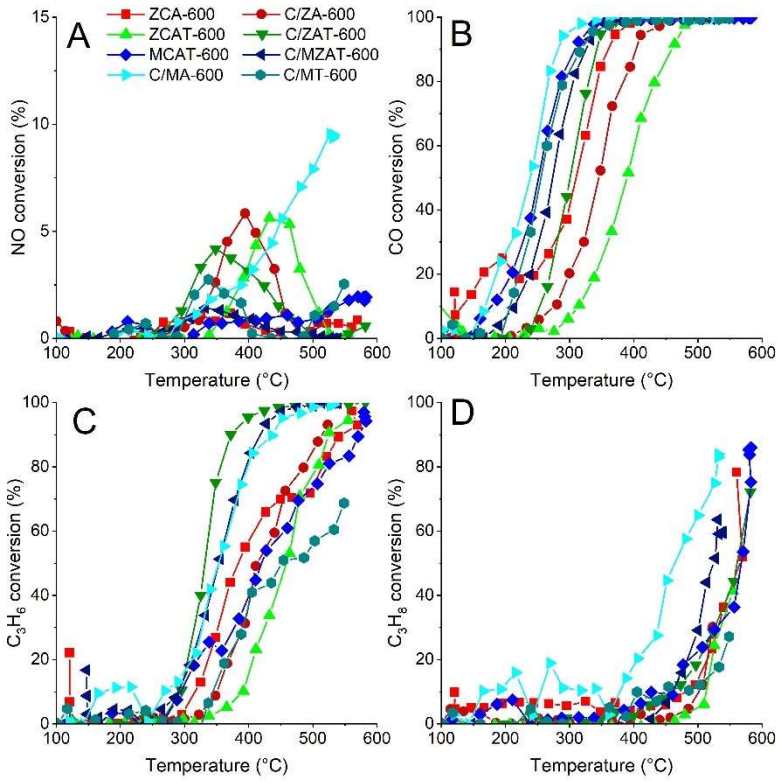

888

889 *Supplementary Figure 11: Temperature programmed conversion curves under stoichiometric conditions, second cycle, A: NO*

890 *conversion, B: CO conversion, C: propene conversion, D: propane conversion.*

891

892

NO conversion discussion

In stoichiometric and lean conditions, all NO reduced during the test is selectively converted to N_2. In the rich condition, NH_3 and N_2O are also formed through side reactions. The selectivity of the NO conversion in the rich condition for all the catalysts is displayed in Supplementary Figure 12 and the corresponding yields can be found in Supplementary Figure 13. The selectivity towards N_2O is very low for all the studied three-way catalysts, however, the selectivities towards N_2 and NH_3 are almost equal at high temperatures. Overall, the yields towards N_2 are higher for the catalysts containing titanium (ZCAT-600, C/ZAT-600, C/MT) as compared to the catalysts that do not contain titanium (ZCA-600, C/ZA-600, C/MA).

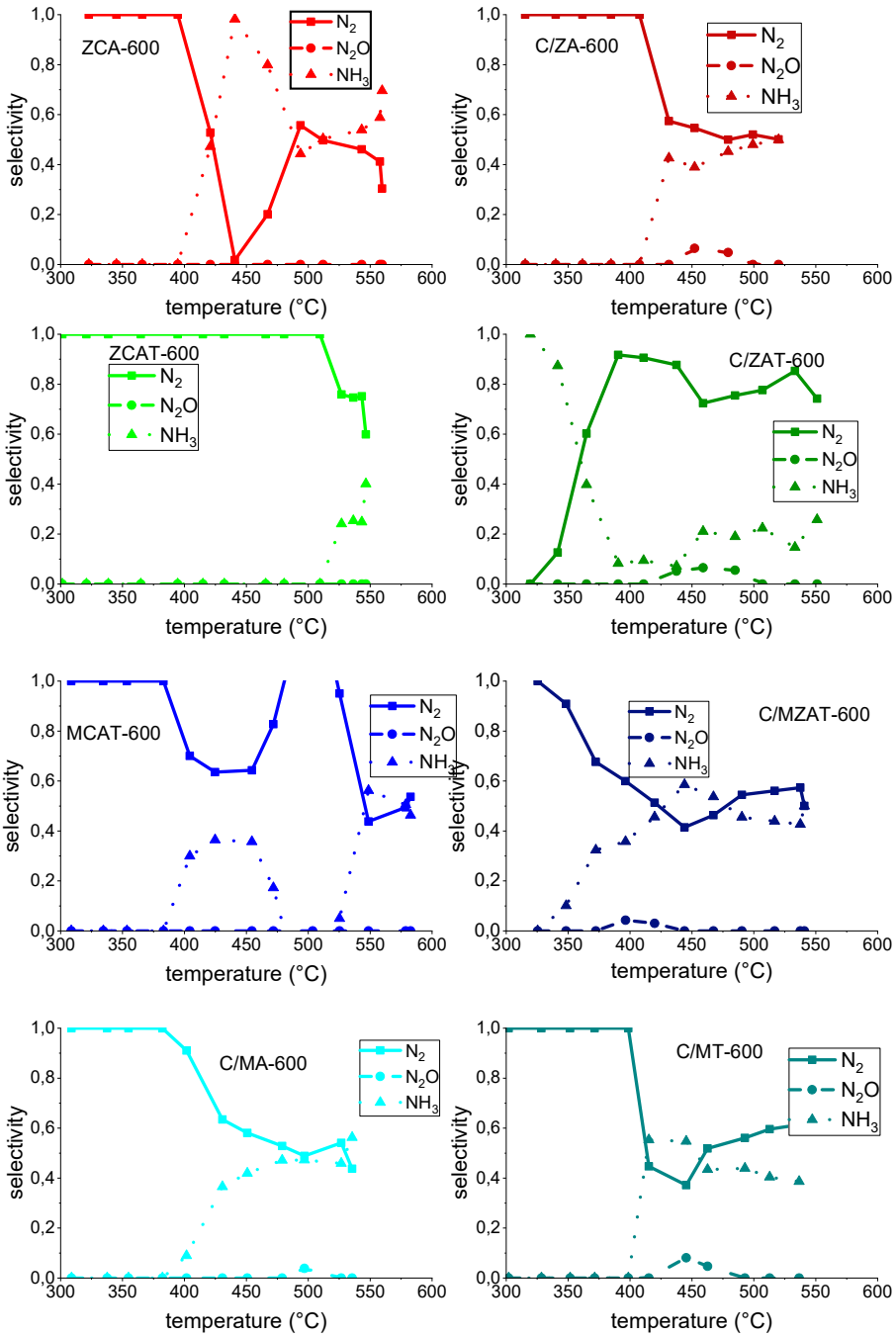

Supplementary Figure 12: Selectivity of NO towards N_2, N_2O and NH_3 during the rich condition for all catalysts.

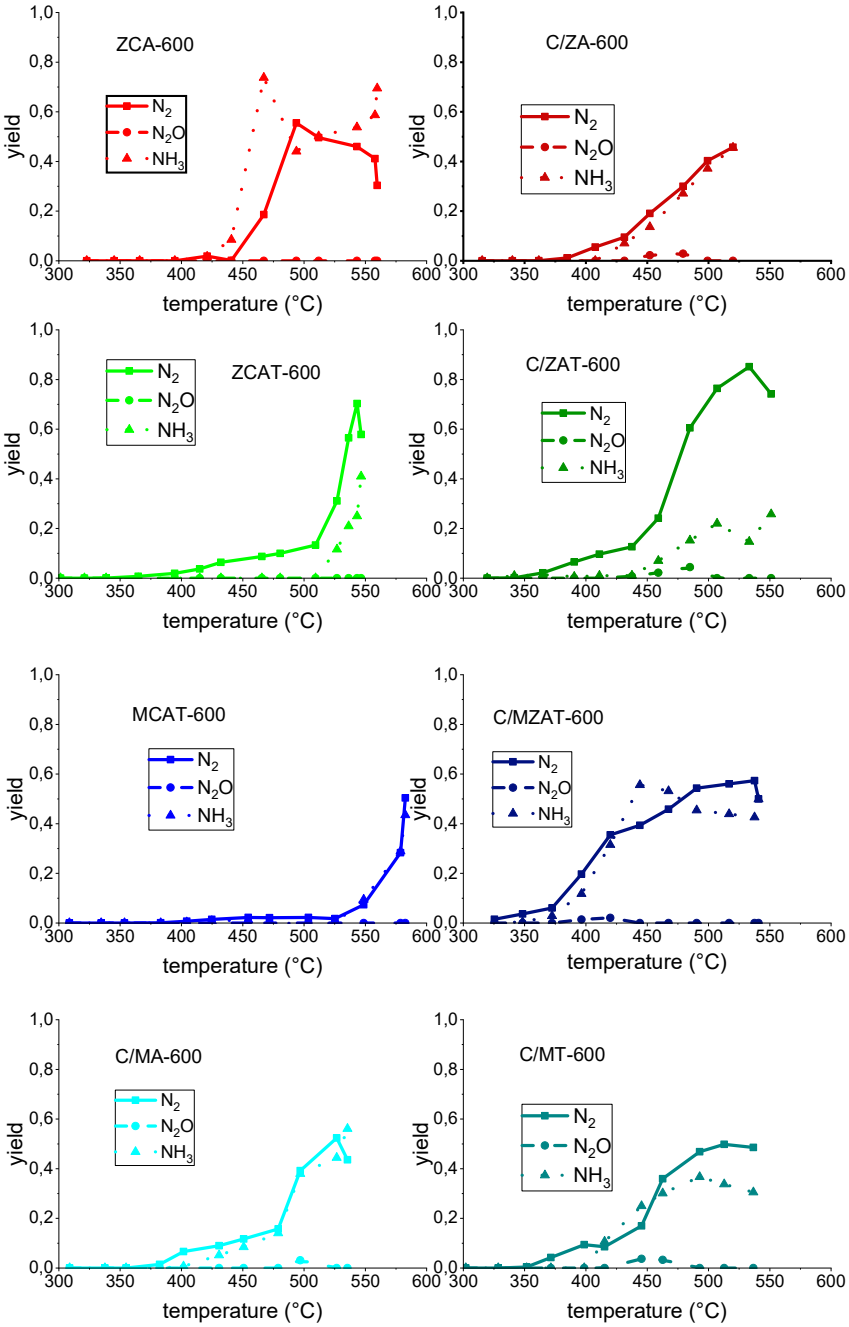

908

909 *Supplementary Figure 13: Yield of NO conversion towards N_2, N_2O and NH_3 for all catalysts.*

910 In stoichiometric and lean conditions, the NO conversion profiles exhibit typical volcano plots.
911 This occurs because the selectivity for the reactions with NO drops for reactions with O_2. In
912 this way, four local maxima for the four different reactants (H_2, CO, propene, propane) can
913 be expected, which explains the often strange shape of the NO conversion profiles. The

914 catalysts used here, under these specific conditions, seem to mainly convert NO with propene
915 or H_2. As an example, for the profile of C/MZAT-600 there is a sharp rise in the NO conversion
916 at around 300°C, which is also the temperature where propene and H_2 conversion starts (H_2
917 conversion profile can be found in Supplementary Figure 14). Analysing the profiles of the first
918 stoichiometric cycle, it suggests that the materials containing titanium produce higher
919 maximal NO conversions. However, while C/MA-600 shows medium conversion at low
920 temperatures, the NO conversion is much higher than for all the other catalysts at high
921 temperatures. This can be related to the propene conversion observed in this case, being less
922 steep than for example C/MZAT-600 and to the propane conversion, which starts at a lower
923 temperature than for the other catalysts. In the lean cycle, the multiple volcano plots are more
924 clear and again, the highest conversion is found for C/MA-600, but C/ZAT and C/MT still stand
925 out to the other catalysts.

926 In the rich conditions, NH_3 formation is also possible (reaction 1) and the selectivity profiles
927 demonstrate that this is certainly the case here. NH_3 formation is also undesired as it is
928 poisonous for the catalyst, corrosive for the system and can form particulate matter (Wang et
929 al., 2015; Nevalainen et al., 2018).

930 $$2\,NO + 5\,H_2 \rightarrow 2\,NH_3 + 2\,H_2O \quad (1)$$

931 However, evaluating the H_2 conversion plots in the rich conditions (Supplementary Figure 15),
932 it can be concluded that the H_2 conversion reaches 100% before the temperature at which the
933 NO conversion starts, mainly due to the reaction with O_2. A source of the extra H_2 required for
934 NH_3 formation can be steam reforming of propene and the water-gas shift reaction (reaction
935 2 and 3) (Mejía-Centeno et al., 2012; Nevalainen et al., 2018).

936 $$C_3H_6 + 3\,H_2O \rightarrow 3\,CO + 6\,H_2 \quad (2)$$

$$CO + H_2O \rightarrow CO_2 + H_2 \quad (3)$$

As concluded above, the three-way catalysts containing titanium have a higher yield for N_2 at high temperatures (500°C) than their titania-free correspondents. Yuan *et al.* postulate that the higher N_2 selectivity of a copper-titanium mixed oxide is due to the existence of more Lewis sites, which adsorb NO as nitrates on the catalyst surface (Yuan et al., 2014).

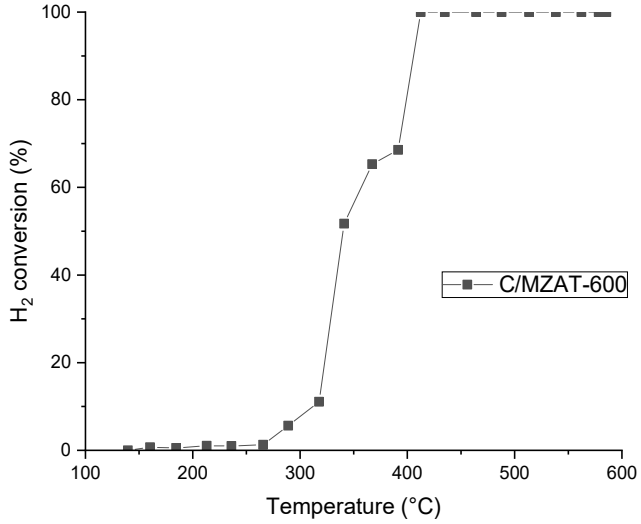

Supplementary Figure 14: H_2 conversion in the first stoichiometric cycle for C/MZAT-600.

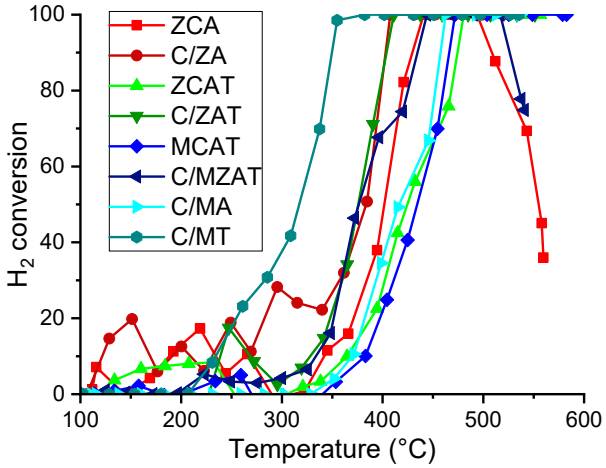

Supplementary Figure 15: H_2 conversion of the materials under rich conditions.

Specific reaction rates and turnover frequency

The conversion profiles presented earlier are proportional to the reaction rates for 200 mg of catalyst at different temperatures. Reaction rates can however also be expressed based on the specific surface area of the catalyst which makes sense as catalysis happens mostly on the surface. A large surface area will give a catalyst advantage over a catalyst with a smaller surface area. For this reason, a specific reaction rate is defined, which expresses the amount of converted molecules per second per m^2 of catalyst surface area. Specific reaction rate profiles for CO, NO and propene in the first stoichiometric cycle can be found in Supplementary Figure 16Supplementary Figure 17Supplementary Figure 18. C/MT-600 and C/MZAT-600, who were already amongst the best performing catalysts, are standing here even more out from the others due to their relatively lower surface area. This shows again that the titania-containing catalysts have a lot of potential but that the small surface area due the crystallisation of titania is a drawback in these high temperature applications.

Another way to express reaction rates is based on the amount of reactive sites in the catalyst, which is called the turnover frequency (TOF). Here it is assumed that the reactive sites are only the Cu-atoms and that every Cu-atom in the material is accessible and taking part in the catalysis. A more accurate TOF would be probably somewhere between the presented TOF and the specific reaction rate as Cu-atoms buried deep into the bulk of the material will most likely not take part in the reactions. Profiles of the TOFs as a function of temperature for CO, NO and propene in the first stoichiometric cycle can be found as Supplementary Figure 19, 19 and 20. As the Cu content for C/MZAT-600, C/MA-600 and C/MT-600 is much lower and their catalytic performance is very good, they stand out even more from the others in the TOF profiles. This emphasizes the fact that Cu deposited as small particles in a post-synthesis method is much more efficient than in a direct synthesis method.

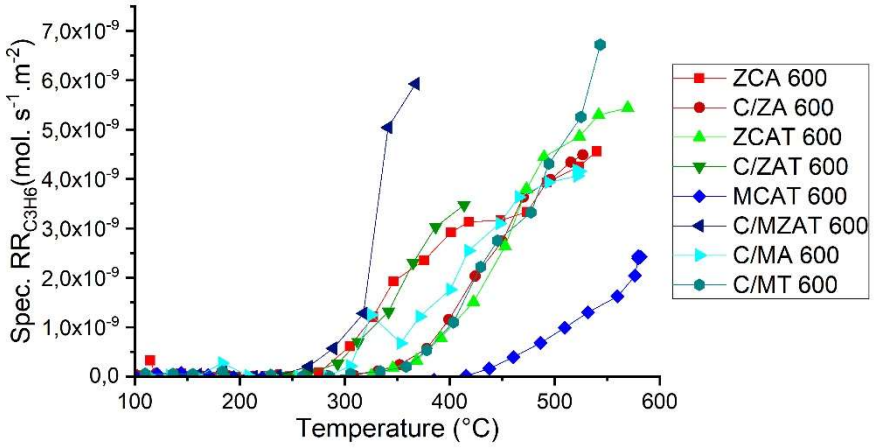

971

972 *Supplementary Figure 16: Specific reaction rates for C_3H_6 during the first stoichiometric cycle.*

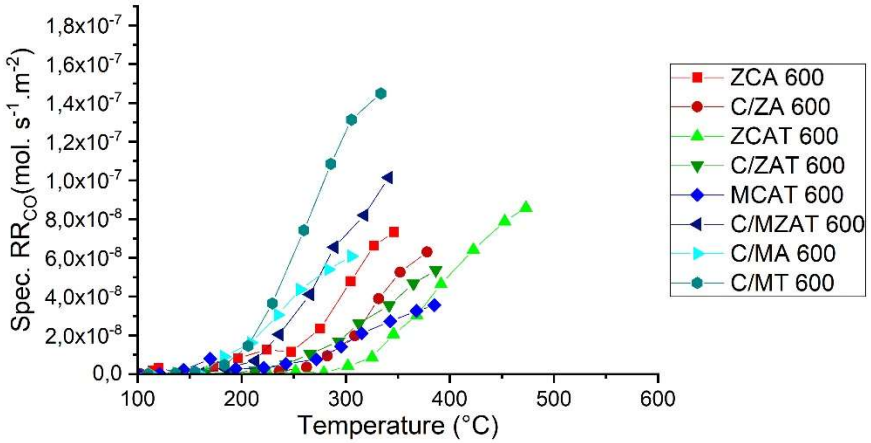

973

974 *Supplementary Figure 17: Specific reaction rates for CO during the first stoichiometric cycle.*

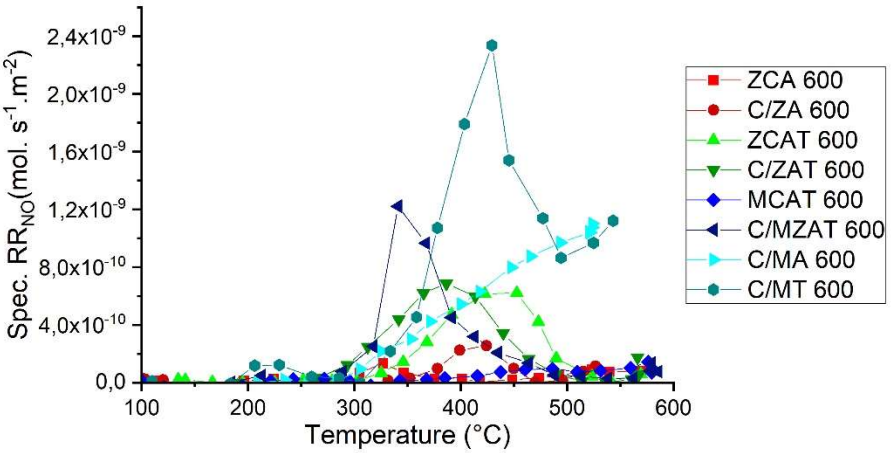

975

976 *Supplementary Figure 18: Specific reaction rates for NO during the first stoichiometric cycle.*

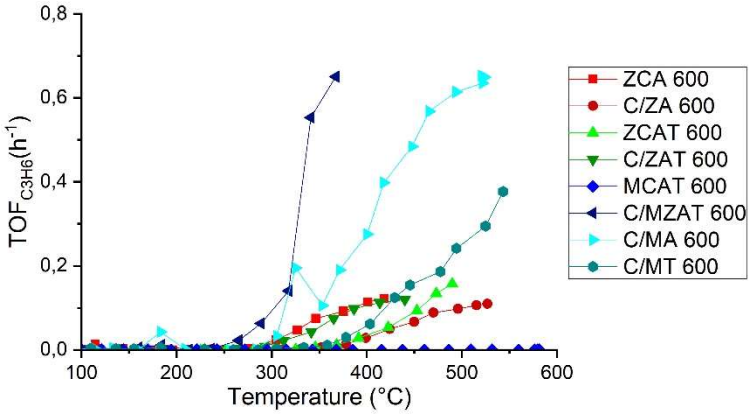

977

978 *Supplementary Figure 19: Turn-over frequencies for C_3H_6 during the first stoichiometric cycle.*

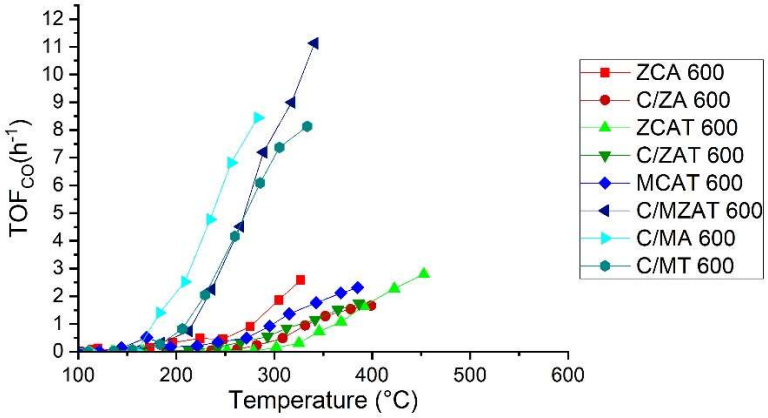

979

980 *Supplementary figure 20 Turn-over frequencies for CO during the first stoichiometric cycle.*

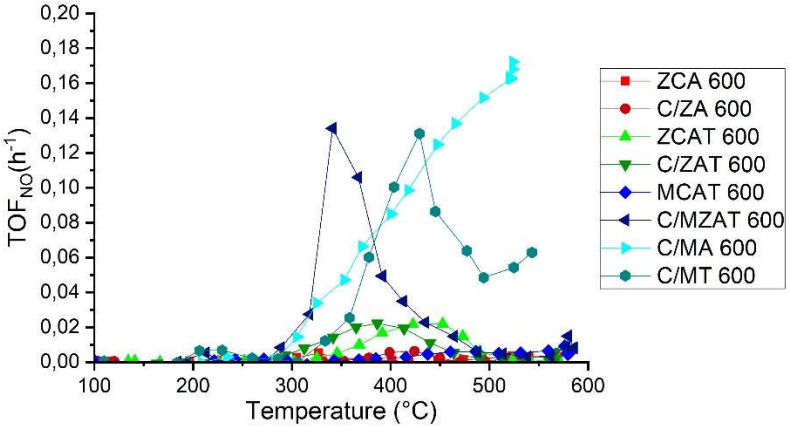

981

982 *Supplementary Figure 21: Turn-over frequencies for NO during the first stoichiometric cycle.*

983

984

Comparison with commercial catalysts

The benchmarking of the catalytic results with literature reports is not that straightforward as small differences in the experimental set-up or in the gas feed compositions may lead to significant differences in the catalytic performances. On the other hand, extensive research in the development and testing of three-way catalysts based on $LaFeO_3$ perovskite materials was performed by the group of P. Granger (Schön et al., 2015, 2017, 2018; Wu et al., 2019) where the catalytic testing was done using the same experimental set-up. The best performing non-PGM containing catalyst in those studies is $La_{0.67}Fe_{0.87}Cu_{0.13}O_3$ and has a T_{50} of 232°C for CO and 386°C for propene in the first stoichiometric cycle but in the second stoichiometric cycle this amounts to 255°C and 390°C. The present developed C/MA-600 three-way catalyst shows a comparable performance for CO conversion in the first stoichiometric cycle (T_{50} = 239°C) and is able to maintain this performance in the second stoichiometric cycle (T_{50} = 239°C). The T_{50} of C/MA-600 for the propene conversion is even improving from the first to the second stoichiometric cycle (from 409 to 353°C), performing much better than the reported perovskite type material. Further, ZCA-600, C/ZA-600, C/ZAT-600 and C/MZAT-600 developed in the present study also show lower T_{50} than the above mentioned perovskite-based catalyst for propene conversion in the second stoichiometric cycle. Remarkably, the current developed three-way catalysts manage to reach in some cases almost 10% NO conversion in stoichiometric conditions, while there is virtually no activity reported using the perovskite type materials. In conclusion, the main advantages of the catalysts developed in this work are the great CO and propene conversion abilities, as well as some NO conversion while also showing a good stability over subsequent catalytic cycles.

Ultimately, to further benchmark the performances of the three-way catalysts developed in this study, two PGM containing commercial three-way catalysts provided by Johnson Matthey

were tested in the same catalytic conditions, namely a 0.5 wt% Pd loaded onto $CeZrO_2$ (results included in the Supplementary Figure 22) and a grounded piece of monolith of the commercial three-way catalytic converter (comm. TWC, results included in Supplementary Figure 23), respectively. For these commercial catalysts, the catalytic testing was performed in all three experimental conditions (stoichiometric, lean, rich) as well as in a second stoichiometric cycle.

It can be observed that for C/MA-600, the CO conversion is almost comparable to that of the commercial TWC, but it is still almost 100°C higher than for $Pd/CeZrO_2$, while the propene conversion needs to be further improved to reach an efficiency comparable with the T_{50} of $Pd/CeZrO_2$. Further, very good results are obtained for the propane conversion, e.g. comparable with the efficiency achieved using the $Pd/CeZrO_2$ commercial catalyst. In terms of NO conversion, lower performances are recorded as compared to the PGM containing catalysts. However, this research demonstrates that the developed materials are very promising for the use in TWC application as noble metal free catalysts, compared to the classical catalysts composition. These new materials have proven to exhibit a considerably good performance for the oxidation of CO, propene and propane.

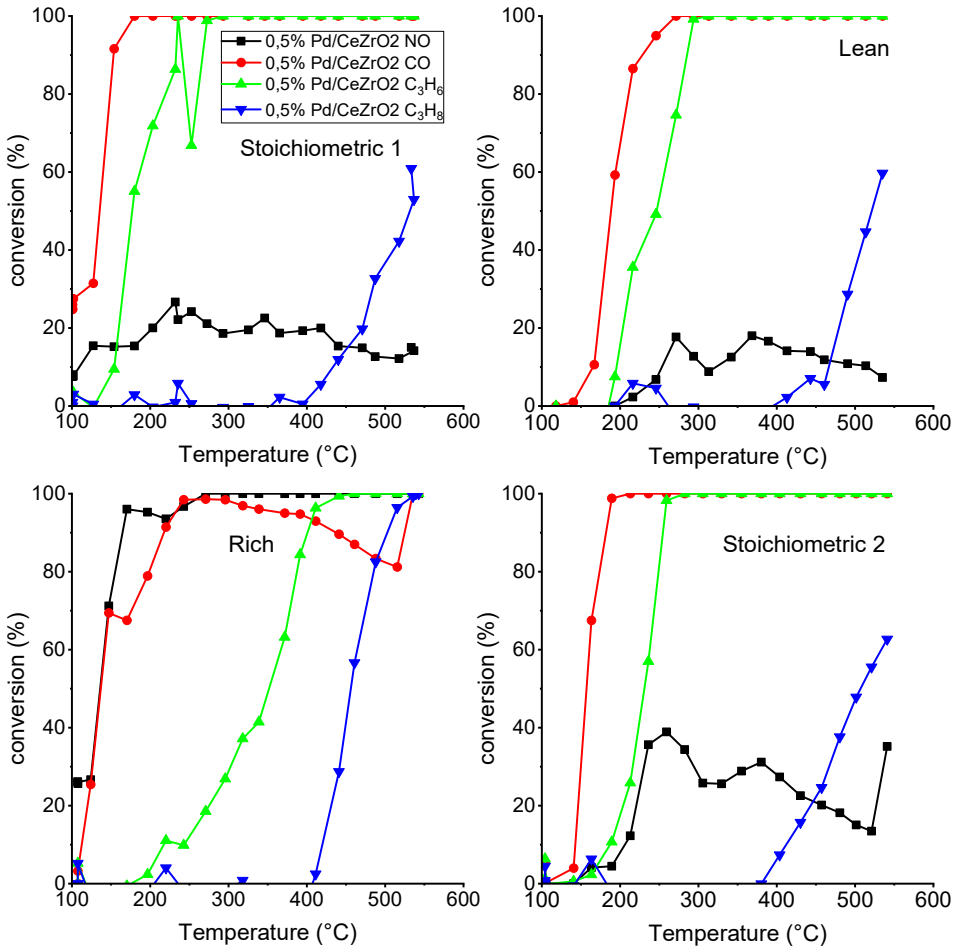

1025

1026 *Supplementary Figure 22: Conversion profiles for 0.5% Pd/CeZrO₂. Top left: first stoichiometric cycle, top right: lean cycle,*

1027 *bottom left: rich cycle, bottom right: second stoichiometric cycle.*

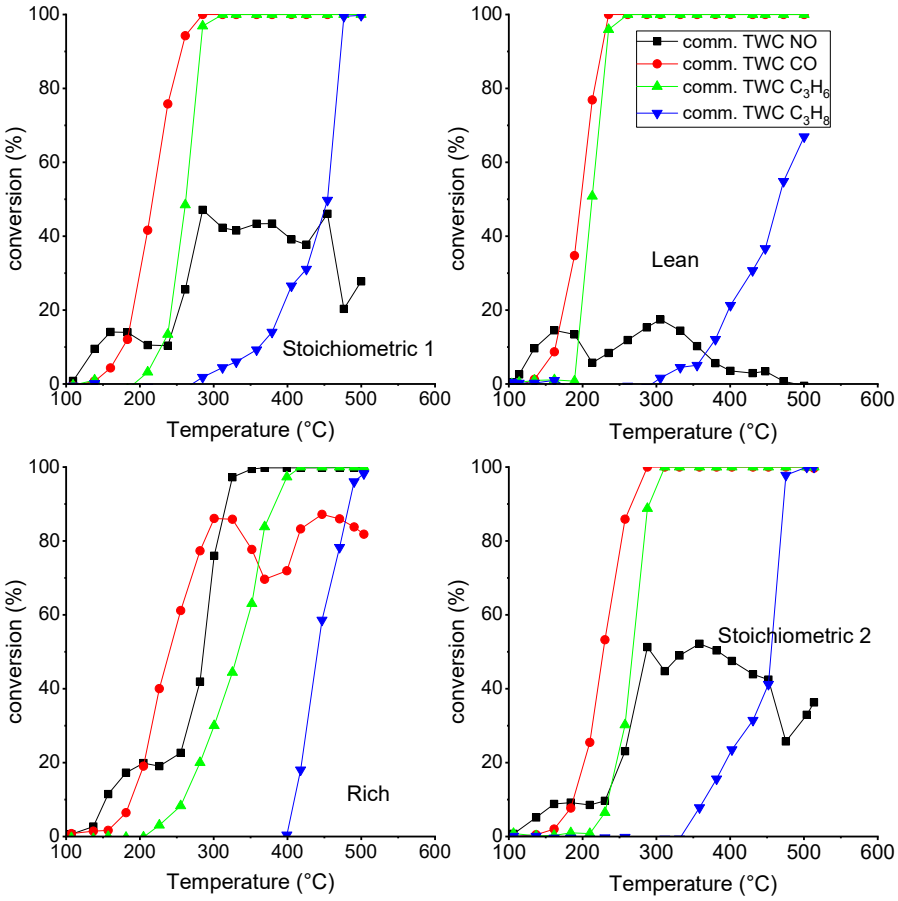

Supplementary Figure 23: Conversion profiles for the commercial TWC catalyst. Top left: first stoichiometric cycle, top right: lean cycle, bottom left: rich cycle, bottom right: second stoichiometric cycle.

Evaluation of the stability of the catalysts and structural investigation of the spent catalysts

In order to verify the stability of the catalysts after the catalytic tests, for the entire series, the XRD patterns were recorded for the used catalysts (Supplementary Figures 24 and 25). No structural modification was observed for the ZCA-600 and C/ZA-600 after the catalytic tests, as the XRD patterns are very comparable, while in the case of ZCAT-600 and C/ZAT-600, the presence of Cu_2O is noticed after the real conditions of the catalytic tests.

Interestingly, the XRD patterns of MCAT-600 before and after the catalytic test associated with the spinel-like structure (initially $Cu_{1.5}Mn_{1.5}O_4$) are shifted. This shift is clearly noticed for the (115) and (044) planes at 57.6° and 63.3° (**¡Error! No se encuentra el origen de la referencia.**26). The newly formed structure is closer to $CuMn_2O_4$ (PDF 00-034-1400), while TiO_2 (rutile) and CuO crystal phases also appear now. For the other three manganese containing materials, a CuO phase is still not detected in the XRD patterns. Similar to the initial analysis, C/MZAT-600 consists again out of the mixed oxide phases of manganese ($CuMn_2O_4$ and $ZnMn_2O_4$), while two new structures appear, namely rutile and a slightly different titanate phase, with an ilmenite ($FeTiO_3$, PDF 00-029-0733) structure. This ilmenite-like system is in this case likely a Zn-doped $MnTiO_3$ composition, for example $Mn_xZn_{1-x}TiO_3$. After the catalytic test, C/MA-600 patterns present features belonging only to Mn_3O_4, while Mn_2O_3 is no longer detected, as before the test. Contrary, the corresponding C/MT-600 consists outof similar components before and after the catalytic test (Mn_3O_4, Mn_2O_3, rutile).

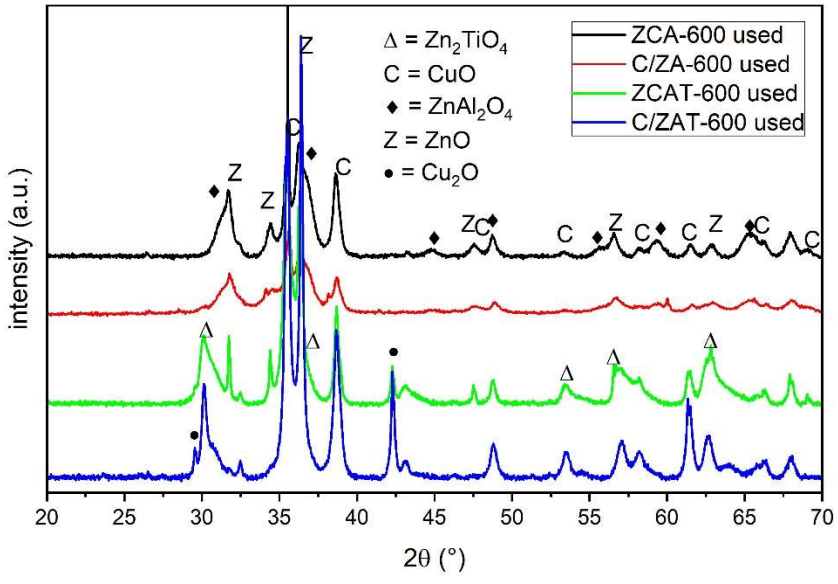

Supplementary figure 24: XRD-patterns of ZCA-600, ZCAT-600, C/ZA-600 and C/ZAT-600 after the catalytic test.

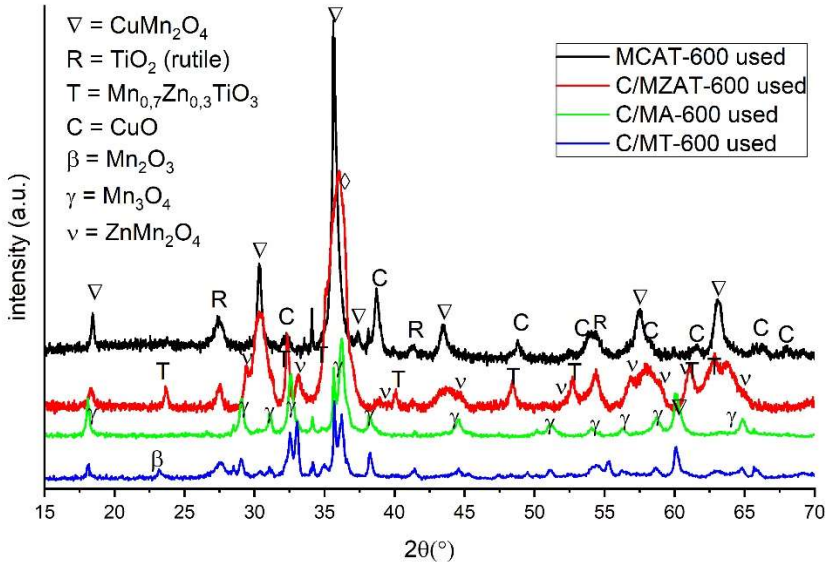

Supplementary figure 25: XRD-patterns of MCAT-600, C/MZAT-600, C/MA-600 and C/MT-600 after the catalytic test.

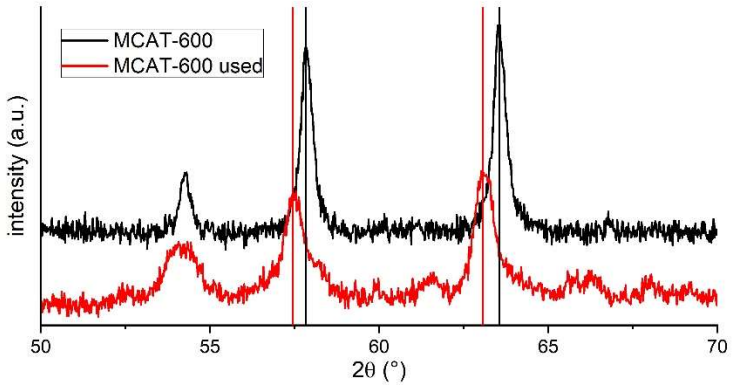

Supplementary figure 26: Detail of the XRD-patterns of MCAT-600 before and after the catalytic test.

References

Mejía-Centeno, I., Castillo, S., Fuentes, G.A., 2012. Enhanced emissions of NH3, N2O and H2 from a Pd-only TWC and supported Pd model catalysts: Light-off and sulfur level studies. Appl. Catal. B Environ. 119–120, 234–240. https://doi.org/https://doi.org/10.1016/j.apcatb.2012.02.030

Nevalainen, P., Kinnunen, N.M., Kirveslahti, A., Kallinen, K., Maunula, T., Keenan, M., Suvanto, M.,

2018. Formation of NH3 and N2O in a modern natural gas three-way catalyst designed for heavy-duty vehicles: the effects of simulated exhaust gas composition and ageing. Appl. Catal. A Gen. 552, 30–37. https://doi.org/https://doi.org/10.1016/j.apcata.2017.12.017

Schön, A., Dacquin, J.-P., Dujardin, C., Granger, P., 2017. Catalytic Activity and Thermal Stability of LaFe1−xCuxO3 and La2CuO4 Perovskite Solids in Three-Way-Catalysis. Top. Catal. 60, 300–306. https://doi.org/10.1007/s11244-016-0615-x

Schön, A., Dacquin, J.-P., Granger, P., Dujardin, C., 2018. Non stoichiometric La1-yFeO3 perovskite-based catalysts as alternative to commercial three-way-catalysts? – Impact of Cu and Rh doping. Appl. Catal. B Environ. 223, 167–176. https://doi.org/https://doi.org/10.1016/j.apcatb.2017.06.026

Schön, A., Dujardin, C., Dacquin, J.-P., Granger, P., 2015. Enhancing catalytic activity of perovskite-based catalysts in three-way catalysis by surface composition optimisation. Catal. Today 258, 543–548. https://doi.org/https://doi.org/10.1016/j.cattod.2014.11.002

Wu, J., Dacquin, J.P., Cordier, C., Dujardin, C., Granger, P., 2019. Optimization of the Composition of Perovskite Type Materials for Further Elaboration of Four-Way Catalysts for Gasoline Engine. Top. Catal. 62, 368–375. https://doi.org/10.1007/s11244-018-1083-2

Wang, J., Chen, H., Hu, Z., Yao, M., Li, Y., 2015. A Review on the Pd-Based Three-Way Catalyst. Catal. Rev. 57, 79–144. https://doi.org/10.1080/01614940.2014.977059

Yuan, D., Li, X., Zhao, Q., Zhao, J., Tadé, M., Liu, S., 2014. A novel CuTi-containing catalyst derived from hydrotalcite-like compounds for selective catalytic reduction of NO with C3H6 under lean-burn conditions. J. Catal. 309, 268–279. https://doi.org/10.1016/j.jcat.2013.09.010